



AFRL-AFOSR-VA-TR-2019-0261

A DNS Study on Hypersonic Boundary-Layer Receptivity and a New Transition Control Strategy by Surface Roughness

Xiaolin Zhong
UNIVERSITY OF CALIFORNIA LOS ANGELES

08/23/2019
Final Report

DISTRIBUTION A: Distribution approved for public release.

Air Force Research Laboratory
AF Office Of Scientific Research (AFOSR)/ RTA1
Arlington, Virginia 22203
Air Force Materiel Command

DISTRIBUTION A: Distribution approved for public release.

REPORT DOCUMENTATION PAGE

*Form Approved
OMB No. 0704-0188*

The public reporting burden for this collection of information is estimated to average 1 hour per response, including the time for reviewing instructions, searching existing data sources, gathering and maintaining the data needed, and completing and reviewing the collection of information. Send comments regarding this burden estimate or any other aspect of this collection of information, including suggestions for reducing the burden, to Department of Defense, Washington Headquarters Services, Directorate for Information Operations and Reports (0704-0188), 1215 Jefferson Davis Highway, Suite 1204, Arlington, VA 22202-4302. Respondents should be aware that notwithstanding any other provision of law, no person shall be subject to any penalty for failing to comply with a collection of information if it does not display a currently valid OMB control number.
PLEASE DO NOT RETURN YOUR FORM TO THE ABOVE ADDRESS.

1. REPORT DATE (DD-MM-YYYY) 08/21/2019	2. REPORT TYPE Final Technical Report	3. DATES COVERED (From - To) 15 August 2015 - 15 MAY 2019
--	---	---

4. TITLE AND SUBTITLE A DNS Study on Hypersonic Boundary-Layer Receptivity and a New Transition Control Strategy by Surface Roughness	5a. CONTRACT NUMBER
	5b. GRANT NUMBER FA9550-15-1-0268
	5c. PROGRAM ELEMENT NUMBER

6. AUTHOR(S) Xiaolin Zhong	5d. PROJECT NUMBER
	5e. TASK NUMBER
	5f. WORK UNIT NUMBER

7. PERFORMING ORGANIZATION NAME(S) AND ADDRESS(ES) Mechanical and Aerospace Engineering Department University of California, Los Angeles Los Angeles, CA 90095	8. PERFORMING ORGANIZATION REPORT NUMBER
--	---

9. SPONSORING/MONITORING AGENCY NAME(S) AND ADDRESS(ES) Air Force Office of Scientific Research AFOSR/NA 4015 Wilson Boulevard, Room 713 Arlington VA 22203-1954 Grant Monitor: Dr. Ivett Leyva	10. SPONSOR/MONITOR'S ACRONYM(S)
	11. SPONSOR/MONITOR'S REPORT NUMBER(S)

12. DISTRIBUTION/AVAILABILITY STATEMENT
Approved for Public Release

13. SUPPLEMENTARY NOTES

14. ABSTRACT
In this report, our research accomplishments are summarized in the DNS study on hypersonic boundary-layer receptivity and a new transition control strategy by surface roughness: 1) DNS study and PSE/LST based theoretical analysis on the fundamental mechanisms of hypersonic boundary-layer instability and receptivity in the context of the relationship between synchronization points and surface roughness location, together with the effects of nose bluntness and thermo-chemical non-equilibrium; 2) a new transition control strategy using surface roughness; 3) a new set of very high-order upwind multi-layer compact (MLC) schemes with spectral-like resolution for hypersonic flow simulations.

15. SUBJECT TERMS

16. SECURITY CLASSIFICATION OF:			17. LIMITATION OF ABSTRACT	18. NUMBER OF PAGES	19a. NAME OF RESPONSIBLE PERSON
a. REPORT	b. ABSTRACT	c. THIS PAGE			19b. TELEPHONE NUMBER (Include area code)
U	U	U	UU	61	

INSTRUCTIONS FOR COMPLETING SF 298

1. REPORT DATE. Full publication date, including day, month, if available. Must cite at least the year and be Year 2000 compliant, e.g. 30-06-1998; xx-06-1998; xx-xx-1998.

2. REPORT TYPE. State the type of report, such as final, technical, interim, memorandum, master's thesis, progress, quarterly, research, special, group study, etc.

3. DATE COVERED. Indicate the time during which the work was performed and the report was written, e.g., Jun 1997 - Jun 1998; 1-10 Jun 1996; May - Nov 1998; Nov 1998.

4. TITLE. Enter title and subtitle with volume number and part number, if applicable. On classified documents, enter the title classification in parentheses.

5a. CONTRACT NUMBER. Enter all contract numbers as they appear in the report, e.g. F33315-86-C-5169.

5b. GRANT NUMBER. Enter all grant numbers as they appear in the report. e.g. AFOSR-82-1234.

5c. PROGRAM ELEMENT NUMBER. Enter all program element numbers as they appear in the report, e.g. 61101A.

5e. TASK NUMBER. Enter all task numbers as they appear in the report, e.g. 05; RF0330201; T4112.

5f. WORK UNIT NUMBER. Enter all work unit numbers as they appear in the report, e.g. 001; AFAPL30480105.

6. AUTHOR(S). Enter name(s) of person(s) responsible for writing the report, performing the research, or credited with the content of the report. The form of entry is the last name, first name, middle initial, and additional qualifiers separated by commas, e.g. Smith, Richard, J, Jr.

7. PERFORMING ORGANIZATION NAME(S) AND ADDRESS(ES). Self-explanatory.

8. PERFORMING ORGANIZATION REPORT NUMBER. Enter all unique alphanumeric report numbers assigned by the performing organization, e.g. BRL-1234; AFWL-TR-85-4017-Vol-21-PT-2.

9. SPONSORING/MONITORING AGENCY NAME(S) AND ADDRESS(ES). Enter the name and address of the organization(s) financially responsible for and monitoring the work.

10. SPONSOR/MONITOR'S ACRONYM(S). Enter, if available, e.g. BRL, ARDEC, NADC.

11. SPONSOR/MONITOR'S REPORT NUMBER(S). Enter report number as assigned by the sponsoring/monitoring agency, if available, e.g. BRL-TR-829; -215.

12. DISTRIBUTION/AVAILABILITY STATEMENT. Use agency-mandated availability statements to indicate the public availability or distribution limitations of the report. If additional limitations/ restrictions or special markings are indicated, follow agency authorization procedures, e.g. RD/FRD, PROPIN, ITAR, etc. Include copyright information.

13. SUPPLEMENTARY NOTES. Enter information not included elsewhere such as: prepared in cooperation with; translation of; report supersedes; old edition number, etc.

14. ABSTRACT. A brief (approximately 200 words) factual summary of the most significant information.

15. SUBJECT TERMS. Key words or phrases identifying major concepts in the report.

16. SECURITY CLASSIFICATION. Enter security classification in accordance with security classification regulations, e.g. U, C, S, etc. If this form contains classified information, stamp classification level on the top and bottom of this page.

17. LIMITATION OF ABSTRACT. This block must be completed to assign a distribution limitation to the abstract. Enter UU (Unclassified Unlimited) or SAR (Same as Report). An entry in this block is necessary if the abstract is to be limited.

REPORT DOCUMENTATION PAGE

Form Approved
OMB No. 0704-0188

The public reporting burden for this collection of information is estimated to average 1 hour per response, including the time for reviewing instructions, searching existing data sources, gathering and maintaining the data needed, and completing and reviewing the collection of information. Send comments regarding this burden estimate or any other aspect of this collection of information, including suggestions for reducing the burden, to Department of Defense, Washington Headquarters Services, Directorate for Information Operations and Reports (0704-0188), 1215 Jefferson Davis Highway, Suite 1204, Arlington, VA 22202-4302. Respondents should be aware that notwithstanding any other provision of law, no person shall be subject to any penalty for failing to comply with a collection of information if it does not display a currently valid OMB control number.
PLEASE DO NOT RETURN YOUR FORM TO THE ABOVE ADDRESS.

1. REPORT DATE (DD-MM-YYYY) 08/21/2019		2. REPORT TYPE Final Technical Report		3. DATES COVERED (From - To) 15 August 2015 - 15 MAY 2019	
4. TITLE AND SUBTITLE A DNS Study on Hypersonic Boundary-Layer Receptivity and a New Transition Control Strategy by Surface Roughness				5a. CONTRACT NUMBER	
				5b. GRANT NUMBER FA9550-15-1-0268	
				5c. PROGRAM ELEMENT NUMBER	
6. AUTHOR(S) Xiaolin Zhong				5d. PROJECT NUMBER	
				5e. TASK NUMBER	
				5f. WORK UNIT NUMBER	
7. PERFORMING ORGANIZATION NAME(S) AND ADDRESS(ES) Mechanical and Aerospace Engineering Department University of California, Los Angeles Los Angeles, CA 90095				8. PERFORMING ORGANIZATION REPORT NUMBER	
9. SPONSORING/MONITORING AGENCY NAME(S) AND ADDRESS(ES) Air Force Office of Scientific Research AFOSR/NA 4015 Wilson Boulevard, Room 713 Arlington VA 22203-1954 Grant Monitor: Dr. Ivett Leyva				10. SPONSOR/MONITOR'S ACRONYM(S)	
				11. SPONSOR/MONITOR'S REPORT NUMBER(S)	
12. DISTRIBUTION/AVAILABILITY STATEMENT Approved for Public Release					
13. SUPPLEMENTARY NOTES					
14. ABSTRACT In this report, our research accomplishments are summarized in the DNS study on hypersonic boundary-layer receptivity and a new transition control strategy by surface roughness: 1) DNS study and PSE/LST based theoretical analysis on the fundamental mechanisms of hypersonic boundary-layer instability and receptivity in the context of the relationship between synchronization points and surface roughness location, together with the effects of nose bluntness and thermo-chemical non-equilibrium; 2) a new transition control strategy using surface roughness; 3) a new set of very high-order upwind multi-layer compact (MLC) schemes with spectral-like resolution for hypersonic flow simulations.					
15. SUBJECT TERMS					
16. SECURITY CLASSIFICATION OF:			17. LIMITATION OF ABSTRACT	18. NUMBER OF PAGES	19a. NAME OF RESPONSIBLE PERSON
a. REPORT	b. ABSTRACT	c. THIS PAGE			19b. TELEPHONE NUMBER (Include area code)
U	U	U	UU	61	

FINAL TECHNICAL REPORT

**A DNS Study on Hypersonic Boundary-Layer Receptivity and a New
Transition Control Strategy by Surface Roughness**

Grant Number: FA9550-15-1-0268

(08/15/2015 to 05/15/2019)

Xiaolin Zhong

Professor

Mechanical and Aerospace Engineering Department

University of California, Los Angeles

Los Angeles, California 90095-1597

phone: (310) 825-2905

e-mail: xiaolin@seas.ucla.edu

Prepared for:

Air Force Office of Scientific Research

AFOSR/NA

4015 Wilson Boulevard, Room 713

Arlington VA 22203-1954

Grant Monitor: Dr. Ivett Leyva/NA

Contents

1	SUMMARY	2
2	RESEARCH OBJECTIVES	3
3	RESEARCH ACCOMPLISHMENTS	4
3.1	DEVELOPMENT OF NEW MULTI-LAYER COMPACT HIGH-ORDER FINITE DIFFERENCE METHODS WITH SPECTRAL-LIKE RESOLUTION FOR COMPRESSIBLE FLOW SIMULATIONS	4
3.2	NUMERICAL STUDY OF 2-D SURFACE ROUGHNESS EFFECTS ON THE SECOND MODE FOR TRANSITION CONTROL OF HYPERSONIC BOUNDARY LAYERS WITH AND WITHOUT REAL GAS EFFECTS	6
3.3	NUMERICAL SIMULATION OF HYPERSONIC BOUNDARY-LAYER INSTABILITY IN A REAL GAS WITH TWO-DIMENSIONAL SURFACE ROUGHNESS	8
3.4	NUMERICAL SIMULATION OF HYPERSONIC FLOW OVER A BLUNT CONE WITH AXISYMMETRIC ISOLATED ROUGHNESS	8
4	NEW MULTI-LAYER COMPACT HIGH-ORDER FINITE DIFFERENCE METHODS WITH SPECTRAL-LIKE RESOLUTION	9
4.1	NEED FOR VERY HIGH-ORDER METHODS	9
4.2	APPLICATIONS IN DNS OF TRANSITION OF HYPERSONIC BOUNDARY LAYERS	12
4.3	OBJECTIVES AND MOTIVATIONS	14
4.4	NEW ONE-DIMENSIONAL MULTI-LAYER COMPACT (MLC) SCHEME	18
4.5	TWO-DIMENSIONAL MLC SCHEME	24
4.6	IMPLEMENTATION OF MLC SCHEME ON EULER AND NAVIER-STOKES EQUATIONS	29
4.7	FOURIER ANALYSIS	37
4.8	SUMMARY OF THE NEW MLC SCHEMES	50
5	PERSONNEL	51
6	PUBLICATIONS	51
7	ACKNOWLEDGEMENT / DISCLAIMER	53
8	REFERENCES	54

1 Summary

The current understanding and research efforts on surface roughness effects in hypersonic boundary-layer flows focus, almost exclusively, on how roughness elements trip a hypersonic boundary layer to turbulence. However, there were a few reports in the literature suggesting that roughness elements in hypersonic boundary-layer flows could sometimes suppress the transition process and delay the formation of turbulent flow. These reports were not common and had not attracted much attention from the research community. Furthermore, the mechanisms of how the delay and stabilization happened were unknown. A study by Duan et al. showed that when 2-D roughness elements were placed downstream of the so-called synchronization point, the unstable second-mode wave in a hypersonic boundary layer was damped. Since the second-mode wave is typically the most dangerous and dominant unstable mode in a hypersonic boundary layer for sharp geometries at a zero angle of attack, this result has pointed to an explanation on how roughness elements delay transition in a hypersonic boundary layer. Such an understanding can potentially have significant practical applications for the development of passive flow control techniques to suppress hypersonic boundary-layer transition, for the purpose of aero-heating reduction. Nevertheless, the previous study was preliminary because only one particular flow condition with one fixed roughness parameter was considered. The previous studies also lacked an examination on the mechanism of the damping effect of the second mode by roughness.

In this report, our research accomplishments are summarized in the DNS study on hypersonic boundary-layer receptivity and a new transition control strategy by surface roughness. First, we conducted DNS study and PSE/LST based theoretical analysis on the fundamental mechanisms of hypersonic boundary-layer instability and receptivity in the context of the relationship between synchronization points and surface roughness location, together with the effects of nose bluntness and thermo-chemical non-equilibrium. Second, we conducted an investigation by means of numerical simulations and PSE/LST analysis on the effects of these fundamental mechanisms on the new transition control strategy using surface roughness. Specifically, we conducted numerical simulations to study the new transition-control method based on surface roughness and wave synchronization by specifying the location, shape, size, height, and distribution density of an array of roughness elements. Both perfect and real-gas flows were considered. Third, we have developed and analyzed a new set of very high-order upwind multi-layer compact (MLC) schemes with spectral-like resolution for hypersonic flow simulations.

The goal is to provide a full physical picture of how and when 2-D roughness elements stabilize a hypersonic boundary layer. Rigorous parametric studies using numerical simulation, linear stability theory (LST), and parabolized stability equation (PSE) are performed to ensure the fidelity of the data and to study the relevant flow physics. All results unanimously confirm the conclusion that the relative location of the synchronization point with respect to the roughness element determines the roughness effect on the second mode. Namely, a roughness placed upstream of the synchronization point amplifies the unstable waves while placing a roughness downstream of the synchronization point damps the second-mode waves. The parametric study also shows that a tall roughness element within

the local boundary-layer thickness results in a stronger damping effect, while the effect of the roughness width is relatively insignificant compared with the other roughness parameters. On the other hand, the fact that both LST and PSE successfully predict the damping effect only by analyzing the meanflow suggests the mechanism of the damping is by the meanflow alteration due to the existence of roughness elements, rather than new mode generation. In addition to studying the unstable waves, the drag force and heating with and without roughness have been investigated by comparing the numerical simulation data with experimental correlations. It is shown that the increase in drag force generated by the Mach wave around a roughness element in a hypersonic boundary layer is insignificant compared to the reduction of drag force by suppressing turbulent flow. The study also shows that, for a cold wall flow, which is the case for practical flight applications, the Stanton number decreases as roughness elements smooth out the temperature gradient in the wall-normal direction. Based on the knowledge of roughness elements damping the second mode gained from the current study, a novel passive transition control method using judiciously placed roughness elements has been developed, and patented, during the course of this research. The main idea of the control method is that, with a given geometry and flow condition, it is possible to find the most unstable second-mode frequency that can lead to transition. By doing a theoretical analysis such as LST, the synchronization location for the most unstable frequency can be found. Roughness elements are then strategically placed downstream of the synchronization point to damp out this dangerous second-mode wave, thus stabilizing the boundary layer and suppressing the transition process. Overall, this research has not only provided details of when and how 2-D roughness stabilizes a hypersonic boundary layer, it also has led to a successful application of numerical simulation data to the development of a new roughness-based transition delay method, which could potentially have significant contributions to the design of future generation hypersonic vehicles.

In addition, we have also developed a new set of very high-order upwind multi-layer compact (MLC) schemes with spectral-like resolution for hypersonic flow simulations. The new methods could be particularly advantageous for numerical simulation of hypersonic boundary layer stability and transition because a wide range of temporal and spatial scales exist in the flow fields.

2 Research Objectives

The objectives of the proposed three-year research project are as follows:

1. To conduct DNS study and PSE/LST based theoretical analysis on the fundamental mechanisms of hypersonic boundary-layer instability and receptivity in the context of the relationship between synchronization points and surface roughness location, together with the effects of nose bluntness and thermo-chemical non-equilibrium.
2. To conduct an investigation by means of numerical simulations and PSE/LST analysis on the effects of these fundamental mechanisms on the new transition control strategy using surface roughness. Specifically, we will conduct numerical simulations to study the new transition-

control method based on surface roughness and wave synchronization by specifying the location, shape, size, height, and distribution density of an array of roughness elements. Both perfect and real-gas flows will be considered.

3. To develop and analyze a new set of very high-order upwind multi-layer compact (MLC) schemes with spectral-like resolution for hypersonic flow simulations.

3 Research Accomplishments

The three-year research project supported by this grant has led to the following publications:

- 3 Ph.D. theses
- 6 archival journal papers
- 13 conference (AIAA) papers

More importantly, the research has produced a large amount of new results, and has led to new understanding of a number of hypersonic boundary layer receptivity mechanisms in the context of surface roughness effects. In the following sections, the major research accomplishments are summarized, followed by a more details discussions of one aspect of our new results from the project.

3.1 Development of new multi-layer compact high-order finite difference methods with spectral-like resolution for compressible flow simulations

Publications: [3-4], [8], [10], [18]

During the three-year project, we developed and analyzed new multi-layer compact high-order finite difference methods with spectral-like resolution for compressible flow simulations. Numerical simulations of multi-scale flow problems such as hypersonic boundary layer transition, turbulent flows, computational aeroacoustics and other flow problems with complex physics require high-order methods with high spectral resolutions. For instance, the receptivity mechanisms in the hypersonic boundary layer are the resonant interactions between forcing waves and boundary-layer waves, and the complex wave interactions are difficult to be accurately predicted by conventional low-order numerical methods. High-order methods, which are robust and accurate in resolving a wide range of time and length scales, are required. Our objective is to develop and analyze new very high-order numerical methods with spectral-like resolution for flow simulations on structured grids, with focus on smooth flow problems involving multiple scales. These numerical methods include: the multi-layer compact (MLC) scheme, the directional multi-layer compact (DMLC) scheme, and the least square multi-layer compact (LSMLC) scheme.

In the first place, a new upwind multi-layer compact (MLC) scheme up to seventh order has been derived in a finite difference framework. By using the ‘multi-layer’ idea, which introduces first derivatives into the MLC schemes and approximates the second derivatives, the resolution of the

MLC schemes can be significantly improved within a compact grid stencil. The auxiliary equations are introduced, and they are the only nontrivial equations. The original equation requires no approximation which contributes to good computational efficiency. In addition, the upwind MLC schemes are derived on centered stencils with adjustable parameters to control the dissipation. Fourier analysis is performed to show that the new MLC schemes have very small dissipation and dispersion in a wide range of wavenumbers in both one and two-dimensional cases, and the anisotropic error is much smaller than conventional finite difference methods in the two-dimensional case. Comparison with discontinuous-Galerkin methods is performed with Fourier analysis as well. Furthermore, stability analysis with matrix method shows that high-order boundary closure schemes are stable because of compactness of the stencils. The accuracies and rates of convergence of the new schemes are validated by numerical experiments of the linear advection equation, the nonlinear Euler equations, and the Navier-Stokes equations in both one and two-dimensional settings. The numerical results show that good computational efficiency, very high-order accuracies, and high spectral resolutions especially on coarse meshes can be attained with the MLC scheme.

On the other hand, even though the MLC scheme is promising in most test cases, it shows weak numerical instabilities for a small range of wavenumbers when it is applied to multi-dimensional flows, which are mainly triggered by the inconsistency between its one and two-dimensional formulations. The instability could lead to divergence in long-time multi-dimensional simulations. Moreover, the cross-derivative approximation in the MLC scheme requires an ad-hoc selection of supporting grid points, and the cross-derivative approximation is relatively inefficient for very high-order cases. To address the remaining challenges of the MLC scheme and achieve better performance for multi-dimensional flow simulations, another two new schemes are developed – the directional multi-layer compact (DMLC) scheme, and the least square multi-layer compact (LSMLC) scheme.

In the second place, a new upwind directional multi-layer compact (DMLC) scheme has been developed for multi-dimensional simulations. The main idea of the DMLC scheme is to introduce auxiliary equation for cross derivative in multi-dimensional cases. Consequently, the spatial discretization can be fulfilled along each dimension independently. With this directional discretization technique, the one-dimensional formulation of the MLC scheme can be applied to all spatial derivatives in a multi-dimensional governing equation. Therefore, the DMLC scheme overcomes the inconsistency between one and two-dimensional formulations of the MLC scheme, and it also avoids the ad-hoc cross-derivative approximations. Two-dimensional Fourier analysis demonstrates that all modes of the DMLC scheme are stable in the full range of wavenumbers, and it has better spectral resolution and smaller anisotropic error than the MLC scheme. Stability analysis with matrix method indicates that stable boundary closure schemes are much easier to be obtained in the DMLC scheme. Numerical tests in the linear advection equation and the nonlinear Euler equations validate that the DMLC scheme are more accurate and require less CPU time than the MLC scheme on the same mesh. In particular, the long-time simulation results reveal that the DMLC scheme is always stable for both periodic and non-periodic boundary conditions in two-dimensional cases.

In the third place, a new upwind least square multi-layer compact (LSMLC) scheme has been developed for multi-dimensional simulations. The main idea of the LSMLC scheme is using the

weighted least square approximation to redesign the two-dimensional formulation for cross derivatives. It avoids the ad-hoc selection of grid points in the MLC scheme. Meanwhile, the two-dimensional upwind scheme can be derived by introducing upwind correction into the weight function. The upwind factor β can adjust the dissipation and stability of the LSMLC scheme. Lagrange multiplier is used to ensure that the LSMLC scheme satisfies both the consistency constraint at the base point and the one-dimensional constraint from the MLC scheme. The LSMLC scheme does not increase computational cost on structured meshes, and can be implemented in the same way as the MLC scheme. A parametric study based on two-dimensional Fourier analysis shows that the truncated Gaussian distribution (TGD) weight function leads to better LSMLC scheme among other weight functions because it removes the numerical instability and maintain small dissipations. The LSMLC scheme has larger dissipation than the MLC scheme, and shows similar spectral resolution. Stability analysis with matrix method indicates that a combination of an interior LSMLC scheme and MLC boundary closure schemes can improve the boundary stability while maintaining small dissipation. Numerical tests in the linear advection equation and the nonlinear Euler equations validate that the LSMLC scheme produces slightly larger errors compared with MLC scheme. The long-time simulation results reveal that the LSMLC scheme is always stable for both periodic and non-periodic boundary conditions in two-dimensional cases.

Overall, the new very high-order multi-layer compact finite difference methods have the properties of simple formulations, high-order accuracies, spectral-like resolutions, and compact stencils, and they are suitable for accurate simulation of smooth multi-scale flows with complex physics. Among the three schemes developed in this dissertation, the DMLC scheme is always the best choice for multi-dimensional simulations because it shows comprehensive improvements from the MLC scheme with consistent stability, higher accuracy and spectral resolution, and better computational efficiency. The LSMLC scheme is also appropriate considering it has consistent stability and it is easy to be implemented.

3.2 Numerical study of 2-D surface roughness effects on the second mode for transition control of hypersonic boundary layers with and without real gas effects

Publications: [1], [20], [22]

The current understanding and research efforts on surface roughness effects in hypersonic boundary-layer flows focus, almost exclusively, on how roughness elements trip a hypersonic boundary layer to turbulence. However, there were a few reports in the literature suggesting that roughness elements in hypersonic boundary-layer flows could sometimes suppress the transition process and delay the formation of turbulent flow. These reports were not common and had not attracted much attention from the research community. Furthermore, the mechanisms of how the delay and stabilization happened were unknown. A recent study by Duan et al. showed that when 2-D roughness elements were placed downstream of the so-called synchronization point, the unstable second-mode wave in a hypersonic boundary layer was damped. Since the second-mode wave is typically the most dangerous and dominant unstable mode in a hypersonic boundary layer for sharp

geometries at a zero angle of attack, this result has pointed to an explanation on how roughness elements delay transition in a hypersonic boundary layer. Such an understanding can potentially have significant practical applications for the development of passive flow control techniques to suppress hypersonic boundary-layer transition, for the purpose of aero-heating reduction. Nevertheless, the previous study was preliminary because only one particular flow condition with one fixed roughness parameter was considered. The study also lacked an examination on the mechanism of the damping effect of the second mode by roughness.

In the current research, we conduct an extensive investigation of the effects of 2-D roughness elements on the growth of instability waves in a hypersonic boundary layer. The goal is to provide a full physical picture of how and when 2-D roughness elements stabilize a hypersonic boundary layer. Rigorous parametric studies using numerical simulation, linear stability theory (LST), and parabolized stability equation (PSE) are performed to ensure the fidelity of the data and to study the relevant flow physics. All results unanimously confirm the conclusion that the relative location of the synchronization point with respect to the roughness element determines the roughness effect on the second mode. Namely, a roughness placed upstream of the synchronization point amplifies the unstable waves while placing a roughness downstream of the synchronization point damps the second-mode waves. The parametric study also shows that a tall roughness element within the local boundary-layer thickness results in a stronger damping effect, while the effect of the roughness width is relatively insignificant compared with the other roughness parameters. On the other hand, the fact that both LST and PSE successfully predict the damping effect only by analyzing the meanflow suggests the mechanism of the damping is by the meanflow alteration due to the existence of roughness elements, rather than new mode generation. In addition to studying the unstable waves, the drag force and heating with and without roughness have been investigated by comparing the numerical simulation data with experimental correlations. It is shown that the increase in drag force generated by the Mach wave around a roughness element in a hypersonic boundary layer is insignificant compared to the reduction of drag force by suppressing turbulent flow. The study also shows that, for a cold wall flow which is the case for practical flight applications, the Stanton number decreases as roughness elements smooth out the temperature gradient in the wall-normal direction.

Based on the knowledge of roughness elements damping the second mode gained from the current study, a novel passive transition control method using judiciously placed roughness elements has been developed, and patented, during the course of this research. The main idea of the control method is that, with a given geometry and flow condition, it is possible to find the most unstable second-mode frequency that can lead to transition. By doing a theoretical analysis such as LST, the synchronization location for the most unstable frequency can be found. Roughness elements are then strategically placed downstream of the synchronization point to damp out this dangerous second-mode wave, thus stabilizing the boundary layer and suppressing the transition process. Overall, this research has not only provided details of when and how 2-D roughness stabilizes a hypersonic boundary layer, it also has led to a successful application of numerical simulation data to the development of a new roughness-based transition delay method, which could potentially have significant contributions to the design of future generation hypersonic vehicles.

3.3 Numerical simulation of hypersonic boundary-layer instability in a real gas with two-dimensional surface roughness

Publications: [9] and [21]

In addition to the roughness effects on the 2-D flat plate with perfect gas assumption, we have also studied the real gas effects for hypersonic applications. Experimental and numerical results have shown that two-dimensional surface roughness can stabilize a hypersonic boundary layer dominated by second-mode instability. We seek to understand how this physical phenomenon extends from an airflow under a perfect gas assumption to that of a real gas. To these ends, a new high-order shock-fitting method that includes thermochemical nonequilibrium and a cut-cell method to handle complex geometries unsuitable for structured body-fitted grids has been developed. The new method is designed specifically for direct numerical simulation of hypersonic boundary-layer transition in a hypersonic real-gas flow with arbitrary shaped surface roughness. The new method is validated and shown to perform comparably to a high-order method with a body-fitted grid. For a Mach 10 flow over a flat plate with a real-gas model, a two-dimensional roughness element was found to stabilize the second mode when placed downstream of the synchronization location, which is consistent with previous research for perfect-gas flows. For a Mach 15 flow over a flat plate, a two-dimensional surface roughness element stabilizes the second-mode instability more effectively in a real gas than in a perfect gas.

3.4 Numerical simulation of hypersonic flow over a blunt cone with axisymmetric isolated roughness

Publications: [11] and [16]

We have also extended the studies of roughness effects on planar 2-D flow to axisymmetric hypersonic flow over slender cones. Specifically, the ability of a finite roughness element to dampen the hypersonic second-mode instability on a cone is explored. A new computer code for simulating discrete roughness using a body-fitted grid over an analytic shape is developed. Linear stability analysis is performed on the Mach 8 meanflow of a 7-degree half-angle straight cone. The resulting N-factor analysis determines the second-mode frequency of 240 kHz to most likely to lead to turbulent transition. A phase velocity plot of the hypersonic modes is obtained and the resulting synchronization location of $s=0.2436$ meters is determined. This led to the design and placement of a roughness element that will effectively dampen the targeted disturbance frequency. An unsteady simulation with a blowing-suction actuator, upstream of the roughness element, introduces a pulse with a nominal frequency content up to 1 MHz. FFT analysis of the pulses history for a roughness case and a no-roughness case are computed and compared. Frequencies 218 kHz and higher are damped while lower frequencies are amplified, effectively showing that the roughness element is able to dampen the target disturbance frequency.

We have also collaborated with Sandia National Laboratory to conduct a joint numerical and experimental investigation of transition-delaying roughness. A numerical simulation was undertaken to design a surface roughness configuration that would suppress Mack's 2nd mode instability in order to maintain laminar flow over a Mach 8 hypersonic blunt cone. Following the design process, the roughness configuration was implemented on a hypersonic cone test article. Multiple experimental runs at the Mach 8 condition with different Reynolds numbers were run, as well as an off-design Mach 5 condition. The roughness did appear to delay transition in the Mach 8 case as intended, but did not appear to delay transition in the Mach 5 case. Concurrently, simulations of the roughness configuration were also computed for both Mach cases utilizing the experimental conditions. Linear stability theory was applied to the simulations in order to determine their boundary layer stability characteristics. This investigation of multiple cases helps to validate the numerical code with real experimental results as well as provide physical evidence for the transition-delaying roughness phenomenon.

4 New Multi-Layer Compact High-Order Finite Difference Methods With Spectral-Like Resolution

One of our major accomplishments of the current research project is the development of new multi-layer compact high-order finite difference methods with spectral-like resolution for compressible flow simulations. The new methods and their analyses are described in detail in this section. Due to space limitation of this report, the detailed results on the other three areas of research accomplishments of the current project are not presented here; they can be found in the cited references stated in Section 3.

4.1 Need for Very High-Order Methods

In the recent few decades, direct numerical simulation (DNS) has become one of the most important methods for the numerical study of various fluid dynamics problems with multiple scales and complex physics. An example is the prediction of the laminar-turbulent transition of hypersonic boundary layers, which is critically important to the development of hypersonic vehicles that are to be used for rapid space access [1]. In general, the transition is a result of the nonlinear response of a laminar boundary layer to various environmental disturbances, but transition mechanisms of hypersonic and supersonic boundary layers are much more complex and much less understood compared with incompressible flows. The transition of hypersonic boundary layers over blunt bodies, which are representative examples, can be affected by the additional effects of shock waves, entropy-layer instabilities, nose bluntness and thermochemical nonequilibrium at high temperatures [2]. As a natural consequence, the DNS of hypersonic boundary layer requires highly accurate numerical methods to resolve a wide range of time and length scales in the flow. At the end of the transition process, the boundary layer becomes fully turbulent, which are more complicated than laminar or transitional flows. The investigation of turbulent flows still face many difficulties because of the strong nonlinearity, the large number of degrees of freedom (DOFs), high sensitivity to small

differences in flow conditions, and many other factors [3]. The numerical simulation of turbulent flows is even more challenging because of the wide range and flat distribution of energy spectrum, and the instantaneous range of scales in turbulent flows increases rapidly with the Reynolds number [4]. However, due to the limitation of computational resources, it is impossible to resolve all the tiny structures in turbulent flows for practical Reynolds numbers. To accurately simulate the turbulent flows, it is required the numerical methods should resolve a significant portion of the scales in the flow fields on feasible grid resolutions. Computational aeroacoustics [5] is another instance which involves complex physics. The generation and propagation of acoustic waves have different features from common aerodynamic problems. In aeroacoustics, the frequency range of acoustic waves is wide, and their amplitude is very small compared with mean flow properties. Meanwhile, flows that generate noises are nonlinear, unsteady and turbulent. These features make the accurate simulation of acoustic wave propagation challenging especially in far-field that requires long-time integration [6]. A common feature of all the flow problems above is the multiple scales embedded in the fields which are difficult to be captured with schemes of low-order accuracy. In the DNS investigation of multi-scale flow problems, the schemes should have very high-order accuracy and high spectral resolution for a wide range of wavelength scales. Moreover, the numerical dissipation and dispersion of such high-order schemes should be low enough to ensure that physical wave components with small amplitude are not suppressed or distorted, which is particularly important in computational aeroacoustics. For reviews of these DNS investigations, one can read [2,4,7–9].

High-order methods have received increasing attention for flow simulations. They have the advantage of achieving the desired accuracy with fewer grid points in the computational domain, improving the computational efficiency, saving the required computer memory, and facilitating large simulations. For these reasons, the high-order methods such as spectral methods, and high-order compact schemes have been commonly used in DNS of turbulent flows [10]. There are many high-order numerical methods developed in the past few decades. Ekaterinaris [11] presented a comprehensive review of the development of high-order methods with low numerical diffusion. Wang [12] discussed high-order methods with emphasize on unstructured grids. Roughly speaking, high-order methods can be classified as linear schemes and nonlinear schemes. Linear schemes, such as spectral methods [13–15], discontinuous-Galerkin (DG) methods [16–19], high-order finite difference methods [20–25], etc., are mainly designed for smooth flows without discontinuities. There exist other flow problems with discontinuities such as shock waves. For simulation of these flows, nonlinear schemes, such as TVD [26,27], ENO [28], WENO [29,30], etc., are designed. These are also hybridizations of linear and nonlinear schemes, which combine the advantages of both methods [31–34].

The conventional numerical methods for multi-scale problems have been the spectral methods [13–15], which are especially suitable for incompressible turbulent flow. Spectral methods use modal basis functions of orthogonal polynomials, such as Fourier series, to represent the solution in the entire computational domain, which leads to very high spectral resolutions and exponential convergence. However, high-order spectral methods have been limited to flows with simple geometries and face difficulties when dealing with complicated boundary conditions. In addition, spectral methods are less accurate for compressible flow problems, such as hypersonic boundary layer

where the critical layer is important.

In an effort to simulate flows over complex geometries more accurately, many discontinuous finite element methods have been developed, such as discontinuous-Galerkin (DG) methods [16–19], spectral difference (SD) methods [35–37], and spectral volume (SV) methods [38–41], etc. These methods use the localized function representation within each element, hence they are suitable to deal with flows over very complex geometries with unstructured grids. Among them, discontinuous-Galerkin (DG) methods may receive the most attention. DG methods combine the characteristics of finite volume methods and finite element methods by using high-order piecewise polynomials within elements and solving numerical fluxes on element interfaces. They have very high-order accuracy and there is no reconstruction needed in DG methods because the entire trial function with multiple degrees of freedom (DOFs) is evolved. Whatever the order of accuracy is, the local stencil can be attained. In other words, each element only interacts with its neighboring elements, which makes DG methods very efficient for parallel computing. However, High-order DG methods have much more degrees of freedom in trial functions, especially for multi-dimensional simulations. Storing and evolving these extra degrees of freedom require larger memory and more CPU time compared with finite volume methods, although they save some computational cost on reconstructions [10].

Compared with other high-order methods, finite difference methods have the advantages of simple formulations and high computational efficiencies with the precondition that the geometry is relatively simple and structured grid can be used. However, conventional explicit finite difference schemes face difficulty in resolving the short waves, which limits their applications in multi-scale problems such as boundary layer transition, turbulent flows, etc. To relax this constraint, finite difference schemes with spectral-like resolution have been widely investigated. The compact finite difference scheme [20,22,24,42–47] is an influential alternative. Lele [20] performed extensive analysis on compact finite difference schemes and showed that through the implicit relation between the derivatives and function values on several grid points, the error in large wavenumber region is reduced and resolutions for short waves are improved. The spectral properties can be further improved by imposing the wavenumber constraints at certain points, i.e., let the modified wavenumber equal to the exact wavenumber at these points. Simultaneously, the maximal truncation order is abandoned on a stencil. Compared with spectral methods, compact schemes are also more flexible with complex geometries and boundary conditions. Lele’s compact schemes have been extended by Chu & Fan [25,47] and Mahesh [22], by introducing the second derivatives in the implicit difference equation. The resulting scheme, which is termed the combined compact difference (CCD) scheme, can achieve higher orders in accuracy and have better spectral resolution than the normal compact schemes on the same stencils. The dispersion-relation-preserving (DRP) scheme [48–52] is another widely used finite difference scheme with spectral-like resolution. Tam and Webb [52] first proposed the DRP scheme by optimizing an explicit finite difference approximation in the wavenumber and frequency space, minimizing the L_2 norm error in modified wavenumbers, hence achieved spectral-like resolution. The general idea of these optimizing finite difference schemes is to lower the error at marginal resolution related to high-frequency wave at the expense of allowing more error for low-frequency wave [53]. Another main difficulty in applying high-order finite difference methods is the numerical instability from boundaries when used on solid wall boundary layer [54]. The stencil is usually wide for high-

order finite difference methods and it is difficult to construct stable boundary closure schemes. In most DNS studies of transitional and turbulent flows of the boundary layer, the orders of numerical methods are often limited due to the numerical instability from boundaries. Many approaches have been proposed to improve the stability of boundary conditions in high-order finite difference methods. Zhong [21] showed that using an adjustable parameter to control dissipation in inner schemes would stabilize the boundary conditions. The non-uniform grid schemes proposed by Zhong and Tatineni [54] use an appropriate grid stretching and cluster grid points near the boundary to attain stable high-order boundary closure schemes. Ashcroft & Zhang [43] and Hixon [44] derived prefactored compact schemes which require smaller stencils and offer simpler boundary condition. By narrowing the grid stencil, the boundary closure schemes can be simplified because narrower boundary stencils are required, which is commonly known as the main advantage of stencil compactness.

The high-order methods discussed above are linear schemes designed for smooth flows. They usually have difficulties in capturing discontinuities, such as shock wave, where they produce spurious oscillations known as the Gibbs phenomenon. For flows with shock, shock-capturing methods based on nonlinear schemes are required. Total-variation-diminishing (TVD) [26], essentially-noscillatory (ENO) [28], and weighted-essentially-noscillatory (WENO) [29] schemes are representative examples of nonlinear schemes. Many advanced nonlinear schemes have been developed from these ideas or their variations [10–12,55,56]. In past twenty years, WENO-based methods receive the most attention among nonlinear schemes. The core idea of WENO scheme is using low-order polynomials and adaptive stencils in reconstruction. The high-order numerical flux or conserved variable is approximated as a weighted summation of low-order polynomials. By using smoothness indicators and automatically selecting the optimal stencil, WENO scheme can achieve very high-order accuracy in the smooth region and maintain nonoscillatory property across shock waves in the discontinuous region. Shu [57] presented a detailed review of the development of high-order WENO schemes. There are three general problems exist in most nonlinear schemes. First, nonlinear schemes are usually computationally inefficient. Second, the accuracy near the shock is reduced because the shock location is only known to $O(h)$ on a finite grid [56]. Last, their performance in the smooth region is not as good as linear schemes due to excessive damping [56]. Although WENO-based schemes can achieve very high-order accuracies in a smooth region, they generate large phase error when resolving small waves in multi-scale flow simulations. In fact, spectral-like resolution can only be achieved by linear schemes as mentioned by Hill & Pullin [58] and Taylor et al. [59]. As a result, these nonlinear schemes may not be accurate enough for DNS studies of hypersonic boundary layers, where short wavelength shock/disturbance interactions need to be resolved with high accuracy [21]. As an alternative approach to deal with shocks, shock-fitting methods [21,60–62] have been used to treat the bow shock as a computational boundary and the flow region behind the shock can be simulated with high-order linear schemes.

4.2 Applications in DNS of Transition of Hypersonic Boundary Layers

The accurate prediction of the laminar-turbulent transition of boundary layers is critically important for hypersonic vehicles because transition has a first-order impact on aerodynamic heating, drag, and vehicle operation [1]. The success of transition prediction relies on a fundamental understanding of the relevant physical mechanisms. Various physical mechanisms of boundary-layer

transition have been reviewed by many authors [63–71] over the years. Most of these reviews are limited to incompressible flows. Compared to incompressible flows, transition mechanisms of hypersonic and supersonic boundary layers are much more complex and much less understood. Reed & Saric [72] reviewed the use of linear stability theory (LST) for transition predictions of compressible boundary layers. Schneider [73–80] had comprehensive reviews on experiments and flight tests of hypersonic boundary. Fedorov [81] summarized the theoretical analysis of hypersonic boundary-layer transition.

Most of our current understanding on hypersonic boundary-layer stability and transition is based on LST. Mack [82] found there exist higher acoustic instability waves, in which the second mode dominates the instability when Mach number is greater than 4. Additional effects that will affect transition and stability of hypersonic boundary layers include shock waves, entropy-layer instabilities, nose bluntness and thermochemical nonequilibrium at high temperature conditions [2]. Fig. 1 presents a schematic of the wave field in a hypersonic flow induced by free-stream disturbance and surface roughness.

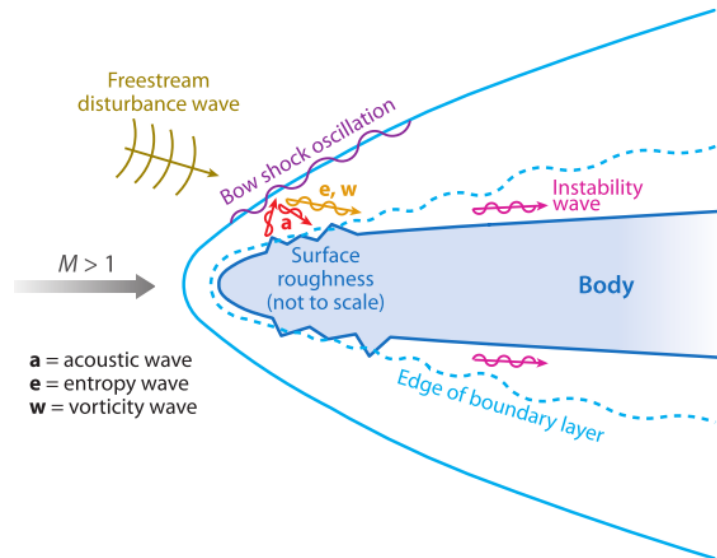


Fig. 1. A schematic of the wave field in a hypersonic flow induced by free-stream disturbance and surface roughness [2].

Along with the developments in high-order numerical methods and computer technologies, direct numerical simulation (DNS) has become a new approach for hypersonic boundary-layer investigations. Kleiser & Zang [83] had a review of DNS research on the transition of wall-bounded shear flows before 1991. They classified these studies into two categories: temporal DNS (TDNS) and spatial DNS (SDNS). TDNS assume the disturbance is periodic in streamwise direction so that only a small domain is needed in the simulation. However, TDNS can't investigate the spatial growth effects of boundary layer. This simplification is mainly due to the limit of computational resources at that time. SDNS uses a much larger domain to conduct the simulation so that it can take the spatial effect into consideration. With the rapid improvement of computational resource, SDNS has become the major approach and significant progress has been made on DNS of hypersonic flow regime through this approach. A recent review on hypersonic boundary-layer transition with focus on the progress of DNS studies was presented by Zhong & Wang [2]. The receptivity, instability, and transition

of hypersonic boundary layers are summarized. Several key points are presented below.

Zhong & Wang [2] mentioned that the main receptivity mechanisms of hypersonic boundary layers are the resonant interactions between forcing waves and boundary-layer which is different from low-speed boundary layers. Free-stream disturbances including acoustic waves, turbulence, and entropy waves are important disturbances for hypersonic vehicles, as shown in Fig. 1. Wall disturbances including blowing suction are also important to the receptivity and instability of hypersonic boundary layers. Together with freestream, they are the main disturbances that hypersonic vehicles experience under real flight conditions. Surface roughness can also alter boundary-layer-instability characteristics substantially and trigger transition within boundary layers. In addition, real gas effects need to be considered at high temperatures and they are found to stabilize the hypersonic boundary-layer flows. When the boundary-layer waves reach a certain amplitude, the nonlinear secondary instabilities and three-dimensional effects lead to breakdown to turbulence with the appearance of turbulent spots in transitional boundary layers. For incompressible boundary layers, secondary instabilities involving fundamental and subharmonic resonances were identified as two relevant mechanisms of boundary-layer transition [67]. For hypersonic boundary layers, although fundamental and subharmonic breakdown mechanisms are both possible, DNS studies have found that they may not be dominant mechanisms because first-mode instabilities are most unstable when they are oblique. There are still many challenging problems in DNS studies of hypersonic boundary layers including three-dimensional and complex boundary-layer investigations, nose-bluntness/entropy-layer effects and transition reversal, theoretical analysis of DNS results, transition control, and others.

4.3 Objectives and Motivations

The objectives of our algorithm development include: (i) developing very high-order schemes with spectral-like resolution for simulation of multi-scale flows, such as hypersonic flows which involve complex physics over simple geometries; (ii) developing new schemes specifically for multi-dimensional flow simulations using novel techniques; (iii) analyzing the properties of the new numerical methods such as stability, dissipation, spectral resolution, and anisotropy; (iv) evaluating the performances of the new numerical methods on linear advection equation, the nonlinear Euler equations and the Navier-Stokes equations in both one and two-dimensional settings including rate of convergence, computational efficiency, and numerical errors, etc.

Currently, the high-order finite difference methods for DNS studies of hypersonic flows are usually upwind schemes or compact schemes with fifth-order accuracy or lower[21]. This dissertation presents a family of new very high-order multi-layer compact (MLC) finite difference methods with spectral-like resolution. The features of these new methods include: (i) the multi-layer framework to reduce stencil size, increase order of accuracy, and improve resolution; (ii) the centered grid stencil for upwind schemes and the adjustable parameter to control numerical dissipation; (iii) the explicit finite difference formula derived on uniform structured grids; (iv) the linear approximation to maintain low computational costs and spectral-like resolution for multi-scale smooth flows; (v) the directional discretization technique for multi-dimensional flow simulations; (vi) the weighted least

square approximation for multi-dimensional flow simulations.

As the main aspect of our new methods, the multi-layer compact finite difference methods in this dissertation refers to a numerical approximation on a layered grid stencil which includes the value layer and derivative layers. Both the value and derivatives are used for approximations of higher derivatives, i.e., every grid point has multiple degrees of freedom (DOFs). Most conventional finite difference and finite volume methods can be considered as mono-layer schemes because the only DOF is the value on every grid point. In our multi-layer scheme, the auxiliary equation is introduced and both value and first derivatives are treated as unknowns. There are two DOFs in one-dimensional simulations, three in two-dimensional simulations, and four in three-dimensional simulations. The original governing equation becomes an exact equation and only approximation for auxiliary equations are required, which is a benefit for computational efficiency. Details of the methods will be presented in forthcoming chapters.

Researchers have developed many numerical methods with multiple degrees of freedom, which is similar to the multi-layer idea in our new scheme. Discontinuous-Galerkin (DG) methods are a typical example, in which the degrees of freedom (DOFs) in each element is determined by the order of accuracy. Orthogonal basis functions are usually utilized to construct the high-order piecewise polynomials within the element, and all the weights of the basis are solved as unknowns. To increase the order, more DOFs are added in each element. All unknowns in DG methods are numerical quantities, so there is no exact equation in the formulations. This feature becomes a major difference in methodology with the new finite difference methods in this dissertation. Spectral difference (SD) methods [35–37] and spectral volume (SV) methods [38–41] also have multiple DOFs in each element, they are similar to DG methods but the way the piecewise polynomials are constructed is different. SV methods define the sub-cells and the averaged conservative variables in these sub-cells are DOFs, while SD methods define the solution points within each element and point values are DOFs [12]. These point or sub-cell values are then used to construct polynomials. DG methods and other finite element methods usually have high-order accuracy and can be easily applied to flow simulations over complex geometries with unstructured grids, and they are very compact because the high-order polynomials are defined, and no reconstructions are required. However, they require a large number of memories, especially in multi-dimensional simulations. In addition, controlling of numerical oscillations in the vicinity of strong discontinuities remains one of challenging issues in these methods.

The idea of evolving multiple degrees of freedom has also appeared in finite volume or finite difference methods. Qiu and Shu, et al. developed a fifth-order Hermite WENO (HWENO) scheme [84–86] in the finite volume framework, where both function value and its first derivative is evolved in time and used in the reconstruction. Balsara et al. [87] also used HWENO approach in their hybrid RKDG+HWENO schemes, where a monotonicity preserving strategy that is scale-free and problem-independent for detecting troubled zones is proposed. They proved that they are good alternatives with lower storage and narrower stencils to Runge-Kutta Discontinuous Galerkin (RKDG) schemes. Luo et al. [88–90] did extensive work on the HWENO schemes with a focus on unstructured grids. They applied HWENO approach as limiters to both original discontinuous-Galerkin (DG) methods

and reconstructed DG methods and found that it can save computational cost, enhance accuracy, and ensure linear stability. The major advantage of these HWENO approaches is compactness of stencils in reconstructions, so they are also very suitable as limiters for discontinuous-Galerkin methods.

There are still many other numerical methods where the use of multiple degrees of freedom can be found. Chang et al. [91–93] proposed the space-time conservation element and solution element (CE/SE) method which includes a unified treatment of spatial and temporal discretization in the space-time domain. The core of the CE/SE method is the two-level, explicit and non-dissipative scheme so the stencil is minimized while maintaining accuracy. Sundar and Yeo [94] designed a meshless method for attaining high-order approximation with compact support by using high-order information at nodes for solution reconstruction. They avoided the trouble of a very large set of supporting points required in conventional meshless methods, thus, successfully increased the accuracy to sixth order. Nishikawa [95–98] developed the first-order hyperbolic system (FOHS) for solving diffusion and advection-diffusion problems. By introducing an additional equation for first derivatives using a relaxation technique, the diffusion term is formulated in a hyperbolic way. An upwind scheme can be applied to the entire system, which leads to a uniform order of accuracy and faster convergence.

In general, the numerical schemes with multiple degrees of freedom (DOFs) attain benefits from their compact support stencil, leading to better efficiency for parallel computing and simpler stable boundary conditions. Most of the methods mentioned above utilized this desirable feature to improve their performance. On the other hand, using multiple DOFs in a linear scheme leads to an additional advantage of a better spectral resolution for small wave components. A prominent explanation can be obtained from Fourier analysis that the resolving ability of a linear scheme depends mainly on degrees of freedom on each grid, i.e. the upper limit of wavenumber (k_{max}) that can be resolved is determined by DOFs (K) through the relation $k_{max} = K\pi$. As mentioned in the previous part of the introduction, it has been a long history to improve spectral resolutions of finite difference methods, and most of the work follows the idea of Lele [20]. They improve the spectral resolution through the implicit relation between derivatives and values in a stencil, but they still face a limit of $k_{max} = \pi$. At the same time, many of these methods comprise the formal order when pursuing better marginal resolution, which is not good for global accuracy. As a comparison, in finite element methods such as discontinuous-Galerkin (DG) methods, the resolution limit k_{max} increases with the order of accuracy benefit from multiple DOFs. This gives us the inspiration to construct a new finite difference method with spectral-like resolution using the multi-layer approach without comprising the order of accuracy. Also, the compact stencil is attained as other numerical methods with multiple DOFs which benefits the construction of boundary closure schemes.

It should be noted that our multi-layer idea differs from the combined compact difference (CCD) scheme [22,25,47] on the role these additional derivatives play and how they are updated. In CCD scheme, the use of second derivatives provides additional implicit relations but does not increase the DOFs. Both first and second derivatives are solved simultaneously from their implicit formulas. While in our new multi-layer compact finite difference methods, the use of the first derivative provides additional DOFs and each DOF is solved separately from a discrete equation. As a result,

the multi-layer idea furtherly improves the resolution. It has been noticed that the first derivative and its auxiliary equation are also used in Nishikawa's method [95–98]. However, the auxiliary equation is derived in a relaxation technique, so the approximation still applies to the first derivatives. While in our new method, the auxiliary equation is derived directly from the original equation by taking its gradients, so the approximation will apply to the second derivatives. As for the motivation, Nishikawa used the first derivative and additional equation to unify the advection and diffusion term, while our purpose is to improve the spectral resolution.

The second aspect of the current multi-layer compact (MLC) finite difference methods is the construction of upwind scheme based on a centered grid stencil with an adjustable parameter to control dissipation. Most high-order finite difference methods used in direct numerical simulation (DNS) are central difference schemes which introduce only phase errors but no dissipative errors in numerical solutions. However, central schemes are not robust enough for convection dominated flows such as supersonic and hypersonic flows. On the other hand, upwind schemes have been widely investigated because of their robustness and they have received much attention in convection dominated flows. In our very high-order upwind MLC schemes, the idea of centered-stencil upwind schemes with an adjustable parameter proposed by Zhong [21] is followed to stabilize the MLC schemes and maintain low dissipation. The main philosophy behind this idea is to attain the upwind schemes so that the dissipative errors are smaller than the dispersive errors inherent in equivalent central schemes and are large enough to stabilize high-order inner schemes coupled with boundary closure schemes. The orders of accuracies of the upwind schemes are one order lower than the highest orders the centered stencils can achieve so that there is an adjustable parameter in the leading dissipative truncation term.

The third aspect of our methods is the use of finite difference approximation based on uniform structured grids. One of the major areas of application of our new methods is the direct numerical simulation of laminar-turbulent boundary layer transition. Although the physics is complex because of a wide range of scales in these flows, the geometries are usually relatively simple such as flat plates, conical cones and blunt bodies with circular or parabolic cross-sections. Smooth curvilinear meshes can be used to discretize the computational domain. So, our new methods are constructed in the finite difference framework which has simple formulations and good computational efficiencies on structured grids.

The fourth aspect of our methods is the use of the linear approximation. As summarized in the previous part of the introduction, high-order linear schemes with spectral-like resolution would be ideal for DNS studies of multi-scale flows in the smooth region. They have smaller dissipation and can achieve better spectral resolution compared with nonlinear schemes. In the simulation for supersonic or hypersonic flow over blunt bodies where the bow shock exists, the smooth region behind the shock can be solved by high-order linear schemes and shock-fitting methods can be applied to capture the bow shocks. In the shock-fitting method of Zhong [21], the bow shock can be treated as a moving computational boundary so that the discontinuity across the shock is avoided. The transient shock location and movement are solved as part of the solutions together with the Navier-Stokes equations. The flow variables immediately behind the shock are determined by Rankine-

Hugoniot relation and a characteristic compatibility equation from the flow field behind the shock. Different variations of shock-fitting methods are discussed in [62]. In the future, the shock-fitting methods can be used to extend the MLC schemes for direct numerical simulation of hypersonic flows.

In summary, the goal of developing the new very high-order finite difference methods with spectral-like resolution is to accurately simulate smooth multi-scale flows with complex physics but over simple geometries. Besides the laminar-turbulent boundary layer transition simulations, these new schemes should also be valuable for other multi-scale flows such as turbulence and computational aeroacoustics. The advantages of these present schemes include, very high-order accuracy and high spectral resolution; simplicity of formulations; compact stencils and simple boundary closure schemes; good computational efficiency.

4.4 New One-Dimensional Multi-Layer Compact (MLC) Scheme

A new very high-order upwind multi-layer compact (MLC) scheme is derived and presented. The model equation of the inviscid Euler equations is linear advection equation, which is used for the derivation of the very high-order MLC scheme. The derivations of the MLC scheme are illustrated in one-dimensional and two-dimensional cases respectively. The implementation of the MLC scheme is discussed, where we apply it to the discretization of inviscid flux term in the Euler equations, and both the inviscid and viscous flux terms in the Navier-Stokes equations. The one and two-dimensional Fourier analysis is then carried out to show the high-order accuracy and spectral-like resolution of the MLC scheme. The effect of adjustable damping parameters in upwind schemes is analyzed, and the comparison with discontinuous-Galerkin methods are also given in one-dimensional cases. In the end, stability analysis for boundary closure schemes are investigated through matrix method.

The one-dimensional advection equation is used to introduce the very high-order upwind MLC scheme for one-dimensional simulations,

$$\frac{\partial u}{\partial t} + c \frac{\partial u}{\partial x} = 0, \quad a \leq x \leq b \quad (0.1)$$

where it is assumed that the wave speed c is a positive constant. Downwind schemes for $c < 0$ can be easily obtained from upwind schemes. The computational domain for one-dimensional wave propagation is a periodic domain in the range of $a \leq x \leq b$, where two boundaries located in $x = a$ and $x = b$ can be either periodic or non-periodic. In the spatial discretization of Eq. (0.1), a uniform mesh with a grid spacing h is used, as presented in Fig. 2. Conventional finite difference schemes use only value u_i in each node to approximate the first derivative $\partial u / \partial x$. Therefore, the grid stencil is usually wide for high-order schemes which could cause difficulty on numerical stability and boundary closure schemes. There are different methods which can reduce stencil size including the influential work of Lele [20].

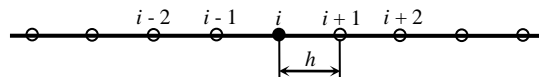


Fig. 2. A uniform mesh for conventional finite difference approximations.

In this chapter, we present a new MLC scheme which achieves both high-order accuracy and high spectral resolution within a compact stencil. In the new methods, the additional governing equation for the first derivatives is introduced by taking the gradient of Eq. (0.1), and the resulting Eq. (0.2) is called the auxiliary equation,

$$\frac{\partial u'}{\partial t} + c \frac{\partial u'}{\partial x} = 0 \quad (0.2)$$

Equations (0.1) and (0.2) form a system of partial differential equations in the following form,

$$\frac{\partial}{\partial t} \begin{bmatrix} u \\ u' \end{bmatrix} = -c \begin{bmatrix} u' \\ u'' \end{bmatrix} \quad (0.3)$$

where u and u' are treated as unknowns. Therefore, there are two degrees of freedom (DOFs) at each grid point. Instead of approximating the first derivative $\partial u/\partial x$ in Eq. (0.1) in conventional finite difference scheme, the MLC schemes only need the approximation of u'' in the right-hand side of Eq. (0.3) to solve the unknowns (u, u'). The original advection equation showed in Eq. (0.1) needs no spatial discretization because u' is solved at each grid point. Therefore, the computational cost is not significantly increased although the MLC scheme involves two equations for the one-dimensional advection problem. To solve the system of equations, finite difference approximation for $u'' (= \partial u'/\partial x)$ in Eq. (0.3) are needed and it can be constructed from u_i and u'_i . Because there are two DOFs at each grid point, higher-order accuracy and better spectral resolution can be obtained in a smaller stencil, which is presented in the following part of this chapter.

Same uniform mesh with grid spacing h , as shown in Fig. 2, is used in the MLC approximations. For a base point i , the approximation of u'' is of the form,

$$\left(\frac{\partial u'}{\partial x} \right)_i = u''_i = \frac{1}{h^2} \sum_{l=-L_1}^{L_2} a_l u_{i+l} + \frac{1}{h} \sum_{m=-M_1}^{M_2} b_m u'_{i+m} - \frac{\alpha}{(p+2)!} u_i^{p+2} h^p + \dots \quad (0.4)$$

$$p = L_1 + L_2 + M_1 + M_2 - 1 \quad (0.5)$$

where there is a summation of u_{i+l} and u'_{i+m} with coefficients a_l and b_m , which can be derived from the Taylor series expansion with respect to base point i . In Eq. (0.4), u_{i+l} , u'_{i+m} , and u''_i are exact solutions at grid points. In the truncation error term, p is the order of accuracy, and α is the coefficient of leading truncation error term. If the truncation error term is taken out, Eq. (0.4) can be considered as a finite difference approximation and u_{i+l} , u'_{i+m} , and u''_i becomes approximate solutions. For simplicity, we use same symbols for exact and approximate variables in this chapter. The corresponding stencil is shown in Fig. 3, which shows a value layer and first derivative layer. A total of L_1+L_2+1 grid points are picked in the value layer, with L_1 points on the upwind side and L_2 points on the downwind side with respect to the base point i . Similarly, M_1+M_2+1 points are used in the derivative layer, with M_1 points on the upwind side and M_2 points on the downwind side. A scheme with this grid stencil is termed the L_1 - L_2 - M_1 - M_2 scheme in this chapter. In the derivation of the inner scheme, the centered stencils ($L_1=L_2, M_1=M_2$) are used, and both upwind schemes and central schemes are constructed on the same centered stencils.

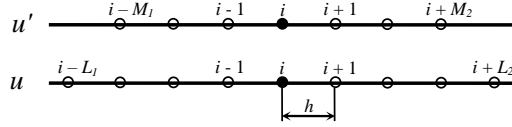


Fig. 3. Stencil of the L_1 - L_2 - M_1 - M_2 scheme for second derivative approximations.

The maximum order that the approximation in Eq. (0.4) can achieve is $L_1+L_2+M_1+M_2$, while in the upwind scheme, p is set to be $L_1+L_2+M_1+M_2-1$, which means the coefficient of the leading truncation term α is a free parameter in the coefficients a_l and b_m . All schemes with nonzero α have a p -th order of accuracy, and the maximum $(p+1)$ -th order is obtained when $\alpha = 0$. The choice of α is not unique, and the value and sign of α play important roles in the magnitude of numerical dissipation and stability of the numerical scheme. The stability of a high-order scheme is critical when applying it to discretize the inviscid flux terms. Meanwhile, deriving a low dissipative upwind scheme is a common goal for accuracy and spectral resolution requirement. Therefore, the value of α needs to be large enough to make the MLC scheme stable and needs to be relatively small to control the dissipation error. Positive or negative α lead to upwind or downwind schemes. It should be noted that the sign of α of upwind schemes varies with the stencils. The idea of adjustable α is similar to what is presented in [21].

Several specific MLC schemes with various orders of accuracy and grid stencils are presented in this section. First, the third-order 1-1-1-1 scheme and the seventh-order 2-2-2-2 scheme are discussed, and they are analyzed and tested comprehensively later in this dissertation. The fifth-order 2-2-1-1 and 1-1-2-2 scheme are also presented, as examples where stencils for value and derivative layers are different.

1-1-1-1 Scheme (3rd Order)

Using a three-point stencil in both value and first derivative layers as shown in Fig. 4, the 1-1-1-1 scheme can be derived as,

$$\left(\frac{\partial u'}{\partial x}\right)_i = u''_i = \frac{1}{h^2} \sum_{l=-1}^1 a_l u_{i+l} + \frac{1}{h} \sum_{m=-1}^1 b_m u'_{i+m} - \frac{\alpha}{5!} u_i^5 h^3 + \dots \quad (0.6)$$

$$\begin{aligned} a_{\pm 1} &= 2 \mp \frac{3}{4} \alpha, & a_0 &= -4, \\ b_{\pm 1} &= \mp \frac{1}{2} + \frac{1}{4} \alpha, & b_0 &= \alpha. \end{aligned} \quad (0.7)$$

where α is the free parameter in coefficients a_l and b_m . The formula leads a third-order upwind scheme when $\alpha > 0$, and it recovers to the fourth-order central scheme when $\alpha = 0$. As a benefit of the multi-layer idea, compactness of grid stencil is achieved. In this case, the third-order upwind scheme or fourth-order central scheme is constructed on the three-point stencil. As a comparison, the grid for conventional finite difference schemes of the same order of accuracy is much wider. For example, a five-point stencil is required in Zhong's third-order upwind scheme or fourth-order central scheme [21].

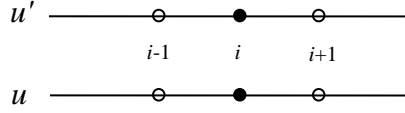


Fig. 4. Stencil of the 1-1-1-1 scheme (3rd order) for second derivative approximations.

Different α values lead to different stability conditions and numerical dissipation which affects accuracy and spectral resolution. Here, the recommended value of α in Eq. (0.7) is chosen based on Fourier analysis results. The value of α for the 1-1-1-1 scheme is 1.5, and the corresponding third-order 1-1-1-1 scheme is,

$$\left(\frac{\partial u'}{\partial x}\right)_i = u_i'' = \frac{1}{h^2} \left(\frac{25}{8} u_{i-1} - 4u_i + \frac{7}{8} u_{i+1} \right) + \frac{1}{h} \left(\frac{7}{8} u'_{i-1} + \frac{3}{2} u'_i - \frac{1}{8} u'_{i+1} \right) \quad (0.8)$$

By choosing some specific α values, the 1-1-1-1 scheme can reduce to upwind schemes on bias stencils. For example, if $\alpha = 2$, then b_1 in Eq. (0.7) is zero and the algorithm reduces to the 1-1-1-0 scheme. Similarly, if $\alpha = 8/3$, then a_1 in Eq. (0.7) is zero and the algorithm reduces to the 1-0-1-1 scheme. Both schemes have larger α values than the recommended value 1.5. Fourier analysis in the next section will show that a larger α leads to more dissipation. Therefore, the upwind scheme on a bias stencil is more dissipative than the 1-1-1-1 upwind scheme on a centered stencil.

2-2-2-2 Scheme (7th Order)

Similarly, using a five-point stencil in both value and first derivative layers as shown in Fig. 5, the 2-2-2-2 scheme can be derived as,

$$\left(\frac{\partial u'}{\partial x}\right)_i = u_i'' = \frac{1}{h^2} \sum_{l=-2}^2 a_l u_{i+l} + \frac{1}{h} \sum_{m=-2}^2 b_m u'_{i+m} - \frac{\alpha}{9!} u_i^9 h^7 + \dots \quad (0.9)$$

$$\begin{aligned} a_{\pm 2} &= \frac{7}{54} \mp \frac{25}{3456} \alpha, & a_{\pm 1} &= \frac{64}{27} \mp \frac{5}{108} \alpha, & a_0 &= -5, \\ b_{\pm 2} &= \mp \frac{1}{36} + \frac{1}{576} \alpha, & b_{\pm 1} &= \mp \frac{8}{9} + \frac{1}{36} \alpha, & b_0 &= \frac{1}{16} \alpha. \end{aligned} \quad (0.10)$$

The formula leads to a seventh-order upwind scheme when $\alpha > 0$, and it recovers to the eighth-order central scheme when $\alpha = 0$. Compactness of grid stencil is significant in this 2-2-2-2 scheme compared with conventional finite difference methods. For example, a nine-point stencil is required in Zhong's seventh-order upwind scheme or eighth-order central scheme [21], while only five points are used in the MLC scheme.

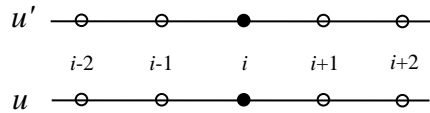


Fig. 5. Stencil of the 2-2-2-2 scheme (7th order) for second derivative approximations.

Again, the recommended value of α in Eq. (0.10) is chosen based on Fourier analysis results.

The recommended value of α for the 2-2-2-2 scheme is 12, and the corresponding seventh-order 2-2-2-2 scheme is,

$$\begin{aligned} \left(\frac{\partial u'}{\partial x}\right)_i = u_i'' = & \frac{1}{h^2} \left(\frac{187}{864} u_{i-2} + \frac{79}{27} u_{i-1} - 5u_i + \frac{49}{27} u_{i+1} + \frac{37}{864} u_{i+2} \right) \\ & + \frac{1}{h} \left(\frac{7}{144} u'_{i-2} + \frac{11}{9} u'_{i-1} + \frac{3}{4} u'_i - \frac{5}{9} u'_{i+1} - \frac{1}{144} u'_{i+2} \right) \end{aligned} \quad (0.11)$$

By choosing some specific α values, the 2-2-2-2 scheme can also reduce to upwind schemes on bias stencils. For example, if $\alpha = 16$, then b_2 in Eq. (0.10) is zero and the algorithm reduces to the 2-2-2-1 scheme. Similarly, if $\alpha = 448/25$, then a_2 in Eq. (0.10) is zero and the algorithm reduces to the 2-1-2-2 scheme. Again, both schemes has larger α values than the recommended value 12, which means they are more dissipative.

2-2-1-1 Scheme (5th Order)

The stencils in the value layer and the derivative layer can be different in the MLC schemes. For example, using five-point stencil for values and three-point stencil for first derivatives as shown in Fig. 6, the 2-2-1-1 scheme can be derived as,

$$\left(\frac{\partial u'}{\partial x}\right)_i = u_i'' = \frac{1}{h^2} \sum_{l=-2}^2 a_l u_{i+l} + \frac{1}{h} \sum_{m=-1}^1 b_m u'_{i+m} - \frac{\alpha}{7!} u_i^7 h^5 + \dots \quad (0.12)$$

$$\begin{aligned} a_{\pm 2} &= \frac{1}{36} \pm \frac{1}{144} \alpha, & a_{\pm 1} &= \frac{20}{9} \pm \frac{7}{36} \alpha, & a_0 &= -\frac{9}{2}, \\ b_{\pm 1} &= \mp \frac{2}{3} - \frac{1}{12} \alpha, & b_0 &= -\frac{1}{4} \alpha. \end{aligned} \quad (0.13)$$

Here, α needs to be negative for upwind schemes. The formula leads to a fifth-order upwind scheme when $\alpha < 0$, and it recovers to the sixth-order central scheme when $\alpha = 0$. The compactness of grid stencil in this 2-2-1-1 scheme is also achieved compared with conventional finite difference schemes. For example, the seven-point stencil is required in Zhong's fifth-order upwind scheme or sixth-order central scheme [21], while only five points are used in the MLC scheme.

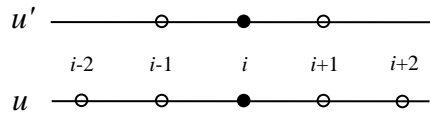


Fig. 6. Stencil of the 2-2-1-1 scheme (5th order) for second derivative approximations.

By choosing some specific α values, the 2-2-1-1 scheme can also reduce to upwind schemes on bias stencils. For example, if $\alpha = -4$, then a_2 in Eq. (0.12) is zero and the algorithm reduces to 2-1-1-1 scheme as,

$$\left(\frac{\partial u'}{\partial x}\right)_i = u_i'' = \frac{1}{h^2} \left(\frac{1}{18} u_{i-2} + 3u_{i-1} - \frac{9}{2} u_i + \frac{13}{9} u_{i+1} \right) + \frac{1}{h} \left(u'_{i-1} + u'_i - \frac{1}{3} u'_{i+1} \right) \quad (0.14)$$

Similarly, if $\alpha = -8$, then b_1 in Eq. (0.12) is zero and the algorithm reduces to 2-2-1-0 scheme as,

$$\left(\frac{\partial u'}{\partial x}\right)_i = u_i'' = \frac{1}{h^2} \left(\frac{1}{12} u_{i-2} + \frac{34}{9} u_{i-1} - \frac{9}{2} u_i + \frac{2}{3} u_{i+1} - \frac{1}{36} u_{i+2} \right) + \frac{1}{h} \left(\frac{4}{3} u'_{i-1} + 2u'_i \right) \quad (0.15)$$

1-1-2-2 Scheme (5th Order)

The stencils in the derivative layer can be wider than that in the value layer in MLC schemes. For example, using three-point stencil for values and five-point stencil for first derivatives as shown in Fig. 7, the 1-1-2-2 scheme can be derived as,

$$\left(\frac{\partial u'}{\partial x}\right)_i = u_i'' = \frac{1}{h^2} \sum_{l=-1}^1 a_l u_{i+l} + \frac{1}{h} \sum_{m=-2}^2 b_m u'_{i+m} - \frac{\alpha}{7!} u_i^{(7)} h^5 + \dots \quad (0.16)$$

$$\begin{aligned} a_{\pm 1} &= \frac{24}{11} \pm \frac{3}{20} \alpha, & a_0 &= -\frac{48}{11}, \\ b_{\pm 2} &= \pm \frac{1}{132} + \frac{1}{600} \alpha, & b_{\pm 1} &= \mp \frac{20}{33} - \frac{17}{300} \alpha, & b_0 &= -\frac{19}{100} \alpha. \end{aligned} \quad (0.17)$$

Like the case of fifth-order 2-2-1-1 scheme, α also needs to be negative for upwind schemes. It should be noted that although both the 1-1-2-2 and 2-2-1-1 schemes have fifth-order of accuracy, their stability can be different. According to our experience in simulations, the 1-1-2-2 scheme would be less stable than 2-2-1-1 scheme. So, it is recommended to use a wider stencil in the value layer, if not the same, than that in the derivative layer.

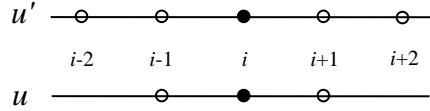


Fig. 7. Stencil of the 1-1-2-2 scheme (5th order) for second derivative approximations.

With one-dimensional MLC schemes, all the spatial derivatives in Eq. (0.3) can be approximated and discretized. The spatial discretization of Eq. (0.3) leads to a system of first-order ordinary differential equations,

$$\frac{d\bar{\mathbf{U}}}{dt} = \mathcal{L}(\bar{\mathbf{U}}, t) \quad (0.18)$$

where $\bar{\mathbf{U}}$ is the discretized flow field variables including function values u_i and first derivatives u'_i , and \mathcal{L} is the approximate operator for spatial discretization through MLC schemes. Time-dependent boundary conditions could be included in Eq. (0.18). The explicit Runge-Kutta schemes can be used to integrate the system of equations in time. For example, the solution procedure from t^n to t^{n+1} using classical fourth-order Runge-Kutta method (RK4) is,

$$\mathbf{k}_1 = dt \mathcal{L}(\bar{\mathbf{U}}^n, t^n) \quad (0.19)$$

$$\mathbf{k}_2 = dt \mathcal{L}\left(\bar{\mathbf{U}}^n + \frac{\mathbf{k}_1}{2}, t^n + \frac{dt}{2}\right) \quad (0.20)$$

$$\mathbf{k}_3 = dt \mathcal{L}\left(\bar{\mathbf{U}}^n + \frac{\mathbf{k}_2}{2}, t^n + \frac{dt}{2}\right) \quad (0.21)$$

$$\mathbf{k}_4 = dt \mathcal{L}(\bar{\mathbf{U}}^n + \mathbf{k}_3, t^n + dt) \quad (0.22)$$

$$\bar{\mathbf{U}}^{n+1} = \bar{\mathbf{U}}^n + \frac{\mathbf{k}_1}{6} + \frac{\mathbf{k}_2}{3} + \frac{\mathbf{k}_3}{3} + \frac{\mathbf{k}_4}{6} \quad (0.23)$$

4.5 Two-Dimensional MLC Scheme

The advection equation is also used as the model equation to illustrate the construction of the very high-order upwind MLC schemes in multi-dimensional cases. The advection equation in three-dimensional flow is,

$$\frac{\partial u}{\partial t} + (\mathbf{c} \cdot \nabla)u = 0 \quad (0.24)$$

where, u is a scalar, and $\mathbf{c} = (c_1, c_2, c_3)$ is a constant vector representing the velocity. For simplicity, only the two-dimensional case is discussed here, and three-dimensional case follows the same methodology. In Cartesian grids, it can be written in scalar form as follows,

$$\frac{\partial u}{\partial t} + c_1 u_x + c_2 u_y = 0 \quad (0.25)$$

Then, two auxiliary equations are introduced by taking derivatives of Eq. (0.25) with respect to x and y ,

$$\frac{\partial(u_x)}{\partial t} + c_1 u_{xx} + c_2 u_{xy} = 0 \quad (0.26)$$

$$\frac{\partial(u_y)}{\partial t} + c_1 u_{xy} + c_2 u_{yy} = 0 \quad (0.27)$$

Equations (0.25) - (0.27) form a system of partial differential equations as follows,

$$\frac{\partial}{\partial t} \begin{bmatrix} u \\ u_x \\ u_y \end{bmatrix} = -c_1 \begin{bmatrix} u_x \\ u_{xx} \\ u_{xy} \end{bmatrix} - c_2 \begin{bmatrix} u_y \\ u_{xy} \\ u_{yy} \end{bmatrix} \quad (0.28)$$

where u , u_x , u_y are treated as unknowns. Therefore, there are three degrees of freedom (DOFs) at each grid point. The system of equations (0.28) is solved by the method of lines simultaneously. Same as the one-dimensional case, the original equation (0.25) needs no approximation because u_x and u_y are part of the solution. On the other hand, u_{xx} , u_{xy} , u_{yy} in auxiliary equations (0.26) and (0.27) need approximations through the MLC schemes. Thus, there are three equations to solve and three terms to approximate, while conventional finite difference method only solves Eq. (0.25) and approximates two terms (u_x , u_y). However, the computational costs are not increased significantly, because much fewer grid points are needed in multi-dimensional simulations with our MLC schemes due to their spectral-like resolutions.

The second derivative terms u_{xx} , u_{yy} in Eq. (0.28) are approximated in the same way as the one-dimensional case. On the other hand, the cross-derivative term u_{xy} , which is not present in one-dimensional MLC schemes, needs to be estimated through another multi-layer approximation based on the similar idea as one-dimensional cases. Discretized function values $u_{i,j}$ and first derivatives $(u_x)_{i,j}$, $(u_y)_{i,j}$ are available for the approximation. Different from one-dimensional MLC schemes, stencils for cross derivatives in two-dimensional MLC schemes are squares in the (x, y) plane, which include the

corner points. Fig. 8 shows the stencil of the L_1 - L_2 - M_1 - M_2 scheme for cross derivatives, where the value layer contains $(L_1+L_2+1)^2$ grid points and the first derivative layer contains $(M_1+M_2+1)^2$ grid points. The centered stencil is used which is similar to one-dimensional stencils. In other words, the base point (i, j) is always located in the center of the square, and both u_x and u_y use the same stencil shown in Fig. 8(b). Consequently, the projection of this stencil on either axis is identical with the stencil for one-dimensional MLC schemes in Fig. 3.

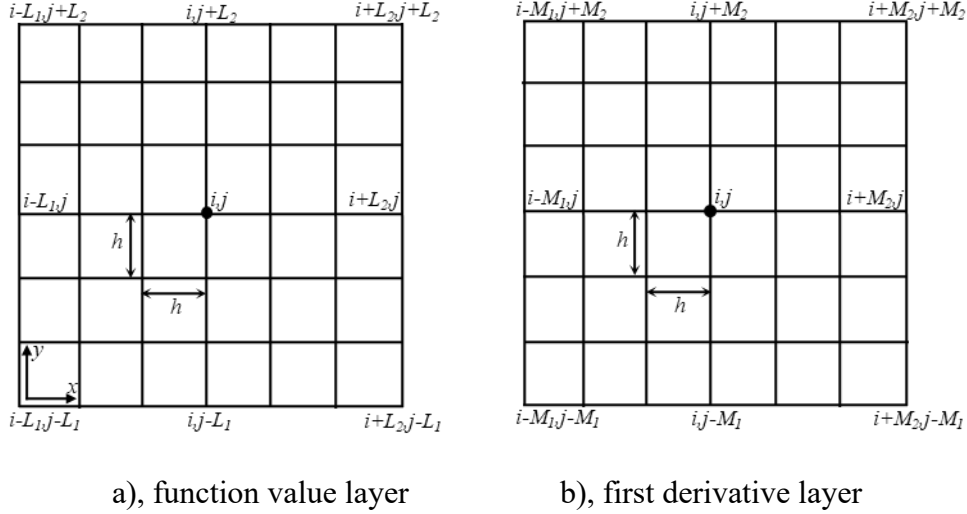


Fig. 8. Stencil of the L_1 - L_2 - M_1 - M_2 scheme for cross derivative approximations.

The approximation can be derived from the following equation,

$$\begin{aligned}
 (u_{xy})_{i,j} = & \frac{1}{h^2} \sum_{\substack{l_x=-L_1 \\ l_y=-L_1}}^{L_2} a_{l_x, l_y} u_{i+l_x, j+l_y} + \frac{1}{h} \sum_{\substack{m_x=-M_1 \\ m_y=-M_1}}^{M_2} b_{m_x, m_y} (u_x)_{i+m_x, j+m_y} + \frac{1}{h} \sum_{\substack{n_x=-M_1 \\ n_y=-M_1}}^{M_2} c_{n_x, n_y} (u_y)_{i+n_x, j+n_y} \\
 & + o(h^{p+1})
 \end{aligned} \tag{0.29}$$

where p is given in Eq. (0.5), and it is the order of corresponding one-dimensional upwind MLC scheme. It is noted that the L_1 - L_2 - M_1 - M_2 scheme has the same maximum order of accuracy in one and two-dimensional case, which is $p+1$. In Eq. (0.29), the scheme with the maximum order of accuracy is derived. The truncation error term is a summation of multiple higher derivatives.

The coefficients a, b, c in Eq. (0.29) can be derived by multivariate Taylor series expansion with respect to base point (i, j) . In the approximations for cross derivatives, there are many freedoms due to redundant points in a square stencil. As a result, the resulting linear system of equations from Taylor series is underdetermined, and the solution of a, b, c is not unique although the maximum order has been used in Eq. (0.29). To get a unique solution, we must preselect supporting points for both values and derivatives before solving the coefficients. In other words, only the coefficients for preselected points are unknowns, and the coefficients for other points are set to be zero. In our derivation, the goal is to find the simplest formula which contains the fewest non-zero terms and the most concise coefficients. On the other hand, only the central scheme is used to approximate the cross derivatives, because the upwind setting for cross derivatives can be cumbersome and complicated. The results of numerical tests in this dissertation show that central schemes for cross derivatives are stable when coupled with one-dimensional upwind schemes. Because they are one order higher than upwind

schemes, they can maintain the overall accuracy of one-dimensional upwind schemes.

Several specific MLC schemes for cross derivatives are presented in this section. Same as the one-dimensional case, the 1-1-1-1 scheme, the 2-2-2-2 scheme, the 2-2-1-1 scheme, and the 1-1-2-2 scheme are derived. All of them are one order higher than their corresponding one-dimensional upwind schemes.

1-1-1-1 Scheme (4th Order)

The stencil to approximate the cross derivative u_{xy} for the 1-1-1-1 scheme is shown in Fig. 9. The maximum order of accuracy achievable in this stencil is 4. To get a unique and simplest solution of coefficients a, b, c in Eq. (0.29), supporting points for values and first derivatives are preselected and marked with black dots in Fig. 9. All the points on the corner are used to provide information of u and all the points along the central x and y lines are used to provide information of u_y and u_x respectively. In total, four value points, two x derivative points, and two y derivative points are preselected. It is noted that the points are distributed symmetrically, which is the requirement of central schemes.

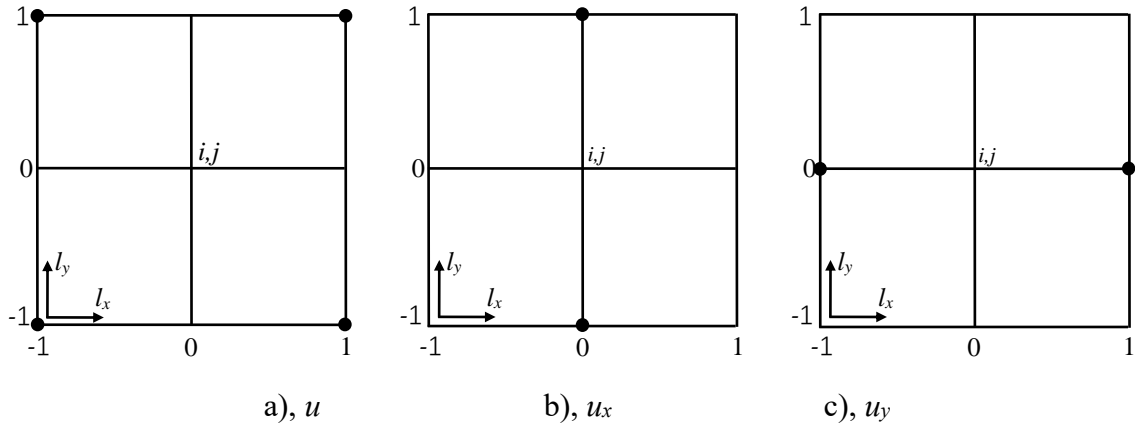


Fig. 9. Stencil and supporting points of the 1-1-1-1 scheme (4th order) for cross derivative approximations.

Using Taylor series expansion, the specific formula for this fourth-order 1-1-1-1 scheme is derived as follows,

$$\begin{aligned}
 (u_{xy})_{i,j} = & \frac{1}{h^2} \left(-\frac{1}{4}u_{i-1,j-1} + \frac{1}{4}u_{i+1,j-1} + \frac{1}{4}u_{i-1,j+1} - \frac{1}{4}u_{i+1,j+1} \right) \\
 & + \frac{1}{h} \left(-\frac{1}{2}(u_x)_{i,j-1} + \frac{1}{2}(u_x)_{i,j+1} \right) + \frac{1}{h} \left(-\frac{1}{2}(u_y)_{i-1,j} + \frac{1}{2}(u_y)_{i+1,j} \right)
 \end{aligned} \tag{0.30}$$

In the derivation of cross derivatives, all possible formulas with the fourth-order accuracy have been searched. It turns out Eq. (0.30) has the simplest form with the fewest non-zero terms and the most concise coefficients.

2-2-2-2 Scheme (8th Order)

Similarly, the stencil and preselected supporting points to approximate the cross derivative u_{xy}

for the 2-2-2-2 scheme are shown in Fig. 10. The maximum order of accuracy achievable in this stencil is 8. A similar methodology is followed as in the 1-1-1-1 scheme to attain the simplest formula. All the points which are not on the central x and y lines are used to provide information of u , and points on central x and y lines are used to provide information of u_y and u_x respectively. In total, sixteen value points, four x derivative points, and four y derivative points are preselected.

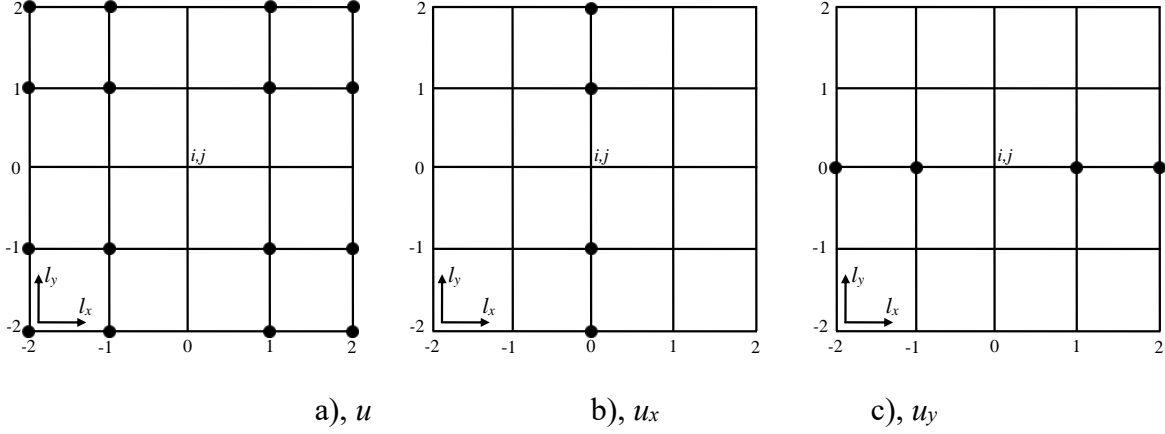


Fig. 10. Stencil and supporting points of the 2-2-2-2 scheme (8th order) for cross derivative approximations.

Using Taylor series expansion, the specific formula for this eighth-order 2-2-2-2 scheme is derived as follows,

$$\begin{aligned}
 (u_{xy})_{i,j} = \frac{1}{h^2} & \left(\begin{aligned} & -\frac{1}{144}u_{i-2,j-2} + \frac{1}{18}u_{i-1,j-2} - \frac{1}{18}u_{i+1,j-2} + \frac{1}{144}u_{i+2,j-2} \\ & + \frac{1}{18}u_{i-2,j-1} - \frac{4}{9}u_{i-1,j-1} + \frac{4}{9}u_{i+1,j-1} - \frac{1}{18}u_{i+2,j-1} \\ & - \frac{1}{18}u_{i-2,j+1} + \frac{4}{9}u_{i-1,j+1} - \frac{4}{9}u_{i+1,j+1} + \frac{1}{18}u_{i+2,j+1} \\ & + \frac{1}{144}u_{i-2,j+2} - \frac{1}{18}u_{i-1,j+2} + \frac{1}{18}u_{i+1,j+2} - \frac{1}{144}u_{i+2,j+2} \end{aligned} \right) \\
 & + \frac{1}{h} \left(\frac{1}{12}(u_x)_{i,j-2} - \frac{2}{3}(u_x)_{i,j-1} + \frac{2}{3}(u_x)_{i,j+1} - \frac{1}{12}(u_x)_{i,j+2} \right) \\
 & + \frac{1}{h} \left(\frac{1}{12}(u_y)_{i-2,j} - \frac{2}{3}(u_y)_{i-1,j} + \frac{2}{3}(u_y)_{i+1,j} - \frac{1}{12}(u_y)_{i+2,j} \right)
 \end{aligned} \tag{0.31}$$

Again, Eq. (0.31) has the simplest form with the fewest non-zero terms and the most concise coefficients among all possible formulas with eighth-order accuracy.

2-2-1-1 Scheme (6th Order)

The stencils for values and derivatives can also be different in two-dimensional MLC schemes as well. For example, 2-2-1-1 scheme has a 25-point square stencil for values and a 9-point square stencil for first derivatives. Consequently, the maximum order of accuracy achievable is 6. The stencil and preselected supporting points to approximate the cross derivative u_{xy} for the 2-2-1-1 scheme are shown in Fig. 11. The way the supporting points are selected here is different from the 1-1-1-1 or 2-2-2-2 schemes. Only the diagonal points are selected as supporting points. In total, eight value points,

four x derivative points, and four y derivative points are preselected.

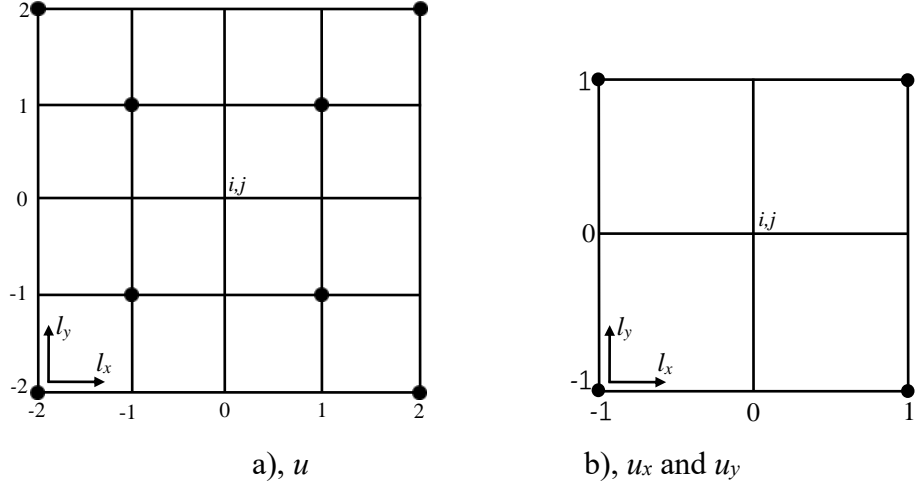


Fig. 11. Stencil and supporting points of the 2-2-1-1 scheme (6th order) for cross derivative approximations.

Using Taylor series expansion, the specific formula for this sixth-order 2-2-1-1 scheme is derived as follows,

$$\begin{aligned}
 (u_{xy})_{i,j} = \frac{1}{h^2} & \left(\frac{1}{144}u_{i-2,j-2} - \frac{1}{144}u_{i+2,j-2} + \frac{5}{9}u_{i-1,j-1} - \frac{5}{9}u_{i+1,j-1} \right. \\
 & \left. - \frac{5}{9}u_{i-1,j+1} + \frac{5}{9}u_{i+1,j+1} - \frac{1}{144}u_{i-2,j+2} + \frac{1}{144}u_{i+2,j+2} \right) \\
 & + \frac{1}{h} \left(\frac{1}{6}(u_x)_{i-1,j-1} + \frac{1}{6}(u_x)_{i+1,j-1} - \frac{1}{6}(u_x)_{i-1,j+1} - \frac{1}{6}(u_x)_{i+1,j+1} \right) \\
 & + \frac{1}{h} \left(\frac{1}{6}(u_y)_{i-1,j-1} - \frac{1}{6}(u_y)_{i+1,j-1} + \frac{1}{6}(u_y)_{i-1,j+1} - \frac{1}{6}(u_y)_{i+1,j+1} \right)
 \end{aligned} \tag{0.32}$$

1-1-2-2 Scheme (6th Order)

Similar to the situation in one-dimensional MLC schemes, we can use a wider stencil in the derivative layer than the value layer. For example, 1-1-2-2 scheme has a 9-point square stencil for values and a 25-point square stencil for first derivatives. The maximum order of accuracy achievable is 6. The stencil and preselected supporting points to approximate the cross derivative u_{xy} for the 1-1-2-2 scheme are shown in Fig. 12. The preselected supporting points are the same as 2-2-1-1 scheme, i.e., only the diagonal points are selected. In total, four value points, eight x derivative points, and eight y derivative points are preselected.

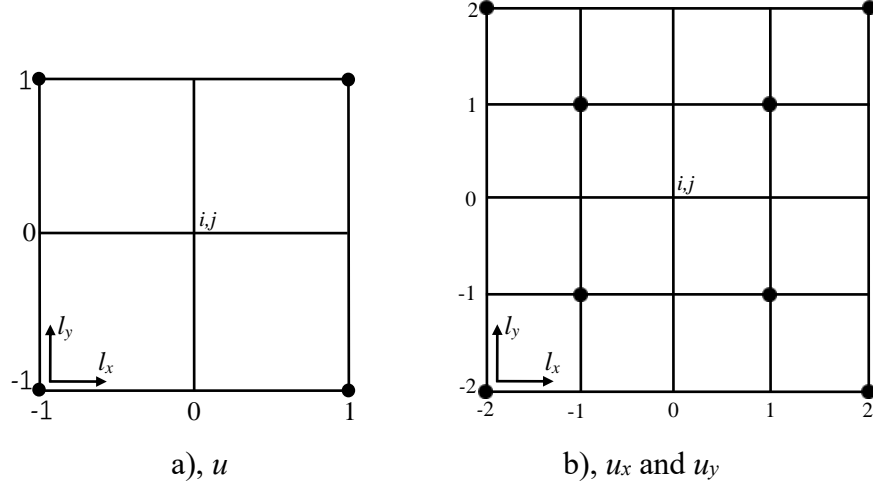


Fig. 12. Stencil and supporting points of the 1-1-2-2 scheme (6th order) for cross derivative approximations.

Using Taylor series expansion, the specific formula for this sixth-order 1-1-2-2 scheme is derived as follows,

$$\begin{aligned}
(u_{xy})_{i,j} = & \frac{1}{h^2} \left(\frac{6}{11}u_{i-1,j-1} - \frac{6}{11}u_{i+1,j-1} - \frac{6}{11}u_{i-1,j+1} + \frac{6}{11}u_{i+1,j+1} \right) \\
& + \frac{1}{h} \left(-\frac{1}{528}(u_x)_{i-2,j-2} - \frac{1}{528}(u_x)_{i+2,j-2} + \frac{5}{33}(u_x)_{i-1,j-1} + \frac{5}{33}(u_x)_{i+1,j-1} \right. \\
& \left. - \frac{5}{33}(u_x)_{i-1,j+1} - \frac{5}{33}(u_x)_{i+1,j+1} + \frac{1}{528}(u_x)_{i-2,j+2} + \frac{1}{528}(u_x)_{i+2,j+2} \right) \\
& + \frac{1}{h} \left(-\frac{1}{528}(u_y)_{i-2,j-2} + \frac{1}{528}(u_y)_{i+2,j-2} + \frac{5}{33}(u_y)_{i-1,j-1} - \frac{5}{33}(u_y)_{i+1,j-1} \right. \\
& \left. + \frac{5}{33}(u_y)_{i-1,j+1} - \frac{5}{33}(u_y)_{i+1,j+1} - \frac{1}{528}(u_y)_{i-2,j+2} + \frac{1}{528}(u_y)_{i+2,j+2} \right)
\end{aligned} \tag{0.33}$$

Although 1-1-2-2 scheme and 2-2-1-1 scheme have the same order of accuracy, Eq. (0.33) has more terms than Eq. (0.32) which means the computational efficiency will be lower, and the coefficients are more trivial. Consistent with one-dimensional MLC scheme, it is recommended to use a wider stencil in the value layer, if not the same, than the derivative layer.

With one-dimensional and two-dimensional MLC schemes, all the spatial derivatives in Eq. (0.28) can be approximated and discretized. Same as one-dimensional case, the spatial discretization of Eq. (0.28) leads to a system of first-order ordinary differential equations. Explicit Runge-Kutta schemes can be applied to the system of equations, and solution procedures are the same as the one-dimensional case.

4.6 Implementation of MLC Scheme on Euler and Navier-Stokes Equations

The compressible viscous flow problems are governed by the Navier-Stokes equations, which can be written in the following conservation-law form in the Cartesian coordinate,

$$\frac{\partial U}{\partial t} + \frac{\partial F_j}{\partial x_j} + \frac{\partial F_{vj}}{\partial x_j} = 0 \quad (0.34)$$

where U , F_j , and F_{vj} are the vectors of conservative variables, inviscid convective flux, and viscous flux in the direction of x_j respectively,

$$U = [\rho, \rho u_1, \rho u_2, \rho u_3, E_t]^T \quad (0.35)$$

$$F_j = \begin{bmatrix} \rho u_j \\ \rho u_1 u_j + p \delta_{1j} \\ \rho u_2 u_j + p \delta_{2j} \\ \rho u_3 u_j + p \delta_{3j} \\ (E_t + p) u_j \end{bmatrix} \quad (0.36)$$

$$F_{vj} = \begin{bmatrix} 0 \\ \tau_{1j} \\ \tau_{2j} \\ \tau_{3j} \\ \tau_{ij} u_i + q_j \end{bmatrix} \quad (0.37)$$

In a wide range of temperature and pressure, the perfect gas assumption can be used, and the total energy per unit volume E_t is calculated from,

$$E_t = \frac{p}{\gamma - 1} + \frac{1}{2} \rho u_k u_k \quad (0.38)$$

In Eq. (0.37), τ_{ij} is the viscous stress which has the form,

$$\tau_{ij} = -\mu \left(\frac{\partial u_i}{\partial x_j} + \frac{\partial u_j}{\partial x_i} \right) - \lambda \frac{\partial u_k}{\partial x_k} \delta_{ij} \quad (0.39)$$

where μ is the molecular viscosity coefficient and λ is second viscous coefficient which is usually assumed to be $-2\mu/3$. The heat flux q_j in Eq. (0.37) is calculated from,

$$q_j = -\kappa \frac{\partial T}{\partial x_j} \quad (0.40)$$

where the heat conductivity coefficient κ is computed through a constant Prandtl number $Pr = 0.72$ as follows,

$$\kappa = \frac{C_p}{Pr} \mu = \frac{\gamma R}{(\gamma - 1) Pr} \mu \quad (0.41)$$

The Navier-Stokes equations reduce to the Euler equations, which are the governing equations for inviscid flows and $F_{vj} = 0$.

The method of lines can be used to discretize the governing equations by separating spatial and temporal discretization. The main difficulty in the spatial discretization is the approximation of the hyperbolic-type convective term in Eq. (0.34), which plays an important role in numerical stability. To construct a stable numerical algorithm, the high-order upwind scheme is commonly utilized to

discretize the convective term. Meanwhile, the elliptic-type viscous flux term in the Navier-Stokes equations can be approximated by high-order central schemes. Therefore, in the remaining part of the chapter, the focus is mainly on the derivation and analysis of the convective term.

Euler Equations

Eliminating the viscous term of Navier-Stokes equations in (0.34) leads to the nonlinear Euler equations for inviscid flows. In the MLC schemes, in addition to the conservative variable U , the derivatives of U are introduced as additional degrees of freedom. Therefore, it is necessary to introduce auxiliary equations as follows,

$$\frac{\partial U_{x_k}}{\partial t} + \frac{\partial F_{jx_k}}{\partial x_j} = 0 \quad (0.42)$$

where the subscript x_k represents a directional derivative in the Cartesian coordinates (x_1, x_2, x_3) . The subscript j is a dummy index. For two and three-dimensional simulation, there are two and three auxiliary equations respectively. The Euler equations and the auxiliary equations can be written in vector forms as follows,

$$\frac{\partial}{\partial t} \begin{bmatrix} U \\ U_{x_k} \end{bmatrix} = - \begin{bmatrix} A_j U_{x_j} \\ F_{jx_k x_j} \end{bmatrix} \quad (0.43)$$

where $A_j = \partial F_j / \partial U$ is the Jacobian matrix and $F_{jxk} = A_j U_{xk}$. The first equation is an exact equation, and only the term F_{jxkxj} in the auxiliary equations needs an approximation. This term is approximated from F_j and F_{jxk} , which can be calculated from U and U_{xk} exactly. Because the operation of Jacobian matrix A_j is expensive, an efficient way to compute F_j and F_{jxk} is to rewrite F_j as a function of conservative variables U as follows,

$$F_j = \begin{bmatrix} U_{1+j} \\ \frac{U_2 U_{1+j}}{U_1} + p \delta_{1j} \\ \frac{U_3 U_{1+j}}{U_1} + p \delta_{2j} \\ \frac{U_4 U_{1+j}}{U_1} + p \delta_{3j} \\ \frac{U_5 U_{1+j}}{U_1} + p \frac{U_{1+j}}{U_1} \end{bmatrix}, \quad p = (\gamma - 1) \left(U_5 - \frac{\sum_{i=2}^4 U_i^2}{2U_1} \right) \quad (0.44)$$

where U_i represents the i th component of U . Then, F_{jxk} can be obtained by taking derivative of Eq. (0.44) to x_k as follows,

$$F_{jx_k} = \begin{bmatrix} U_{1+jx_k} \\ \frac{(U_{2x_k} U_{1+j} + U_2 U_{1+jx_k}) U_1 - U_2 U_{1+j} U_{1x_k}}{U_1^2} + p_{x_k} \delta_{1j} \\ \frac{(U_{3x_k} U_{1+j} + U_3 U_{1+jx_k}) U_1 - U_3 U_{1+j} U_{1x_k}}{U_1^2} + p_{x_k} \delta_{2j} \\ \frac{(U_{4x_k} U_{1+j} + U_4 U_{1+jx_k}) U_1 - U_4 U_{1+j} U_{1x_k}}{U_1^2} + p_{x_k} \delta_{3j} \\ \frac{(U_{5x_k} U_{1+j} + U_5 U_{1+jx_k}) U_1 - U_5 U_{1+j} U_{1x_k}}{U_1^2} + p_{x_k} \frac{U_{1+j}}{U_1} + p \frac{U_{1+jx_k} U_1 - U_{1+j} U_{1x_k}}{U_1^2} \end{bmatrix} \quad (0.45)$$

$$p_{x_k} = (\gamma - 1) \left(U_{5x_k} - \frac{\sum_{i=2}^4 U_i U_{ix_k}}{U_1} + \frac{U_{1x_k} \sum_{i=2}^4 U_i^2}{2U_1^2} \right)$$

In this form, F_{jxk} is only a function of U and U_{xk} which are the unknowns in Eq. (0.43).

After F_j and F_{jxk} are obtained from Eqs. (0.44) and (0.45), the new MLC schemes are applied to numerically approximate F_{jxkxj} in Eq. (0.43). Specifically, the one-dimensional MLC scheme in Eq. (0.4) is used when $j = k$, and the two-dimensional MLC scheme in Eq. (38) is used when $j \neq k$. For the case of $j = k$, the upwind MLC schemes are applied through flux splitting methods. In this section, a locally global Lax-Friedrichs approach is designed, which is similar to the flux splitting in Zhong's upwind schemes [21]. The inviscid flux F_j and their derivatives F_{jxk} , F_{jxkxj} are decomposed into positive and negative wave fields as follows,

$$\begin{aligned}
F_j &= F_j^+ + F_j^- \\
F_{jx_k} &= F_{jx_k}^+ + F_{jx_k}^- \\
F_{jx_kx_j} &= F_{jx_kx_j}^+ + F_{jx_kx_j}^-
\end{aligned} \quad (0.46)$$

The positive part F_j^+ and negative part F_j^- are approximated by the upwind and downwind MLC schemes respectively, which have the same formula given in Eq. (0.4), but the opposite sign in α . It is required that the flux F_j^+ and F_j^- contains only positive and negative eigenvalues in their Jacobian matrices respectively. A straightforward approach to construct F_j^+ and F_j^- and their derivatives are,

$$F_j^+ = \frac{1}{2}(F_j + \Lambda U), \quad F_j^- = \frac{1}{2}(F_j - \Lambda U) \quad (0.47)$$

$$F_{jx_k}^+ = \frac{1}{2}(F_{jx_k} + \Lambda U_{x_k}), \quad F_{jx_k}^- = \frac{1}{2}(F_{jx_k} - \Lambda U_{x_k}) \quad (0.48)$$

where, λ is a positive parameter large enough to make F_j^+ and F_j^- to contain only positive and negative eigenvalues. In Zhong's upwind schemes, λ is a local parameter, which introduces small dissipation. However, local λ causes difficulty for the new MLC schemes because λ needs to be constant for the splitting of F_{jxk} in Eq. (0.48). On the other hand, using a constant λ in the entire domain will introduce large dissipation especially for low order methods such as the third-order 1-1-1-1 scheme. Therefore, in our locally global Lax-Friedrichs approach, a constant λ within each stencil is used, which has the form,

$$\Lambda = \max(\lambda_\tau) \quad (0.49)$$

and λ_i is a positive parameter chosen to be larger than the local maximum eigenvalues of the Jacobian A_j on point i . When the Euler equations are discretized at a base point i_0 , λ is set to be the largest λ_i in the grid stencil. Taking one-dimensional 2-2-2-2 scheme as an example, at the point i_0 , the largest λ_i of the five supporting points ($i_0-2 < i < i_0+2$) in the stencil is chosen to be λ . The procedure is repeated for every base point. Compared with using a constant λ in the entire domain, the locally global Lax-Friedrichs approach has the benefit of maintaining low dissipation. For cross derivatives ($j \neq k$), the central schemes are applied to F_{jxkxj} directly for better computational efficiency. After the MLC approximations, Eq. (0.43) becomes a system of ordinary differential equations, which can be solved by the Runge-Kutta methods.

The discretization described above is performed with respect to the Cartesian coordinates (x_1, x_2, x_3), and this is straightforward for rectangular physical domains. In general case, the physical domain can have different shapes where curvilinear meshes are required. Therefore, a coordinate transformation between physical and computational domain (ξ_1, ξ_2, ξ_3) will be applied to the governing equations. The discretization with MLC schemes can be applied in the computational domain, which is very similar to the description above. The details of the transformation are not included for the sake of length.

The boundary conditions of both U and U_{xk} are needed when the MLC schemes are applied to the Euler equations (0.43) in a flow simulation with physical boundaries. Most approaches from other finite difference methods still apply to the boundary conditions of U . However, the boundary conditions of U_{xk} needs to be dealt with in different manners. It should be noted that the boundary condition itself is a big subject, and the optimal boundary conditions for the MLC schemes still need further investigation. Here, only one practicable way from many approaches is briefly described. For simplicity, illustration is given for two-dimensional simulations.

It is usually easier to derive boundary conditions on the primitive variables $V = (\rho, u, v, p)^T$ instead of U . Fig. 13 shows a physical boundary along the x -direction, where the boundary value V , the tangential derivative V_x , and the normal derivative V_y need to be determined. The derivative boundary conditions can be obtained through governing equations. The Euler equations in two-dimensional case can be written in the primitive form,

$$(A_2 T) V_y = -(A_1 T) V_x - T V_t \tag{0.50}$$

where the A_1 and A_2 are the Jacobians, and T is defined as $\partial U / \partial V$. The matrices A_1, A_2 , and T are only functions of V . If the values of V, V_x , and V_t are available on the boundaries, then V_y can be obtained by solving Eq. (0.50). Therefore, the core problem in boundary conditions becomes determining V, V_x , and V_t on the boundaries. This idea can be applied to different types of boundaries. Some examples are given below.

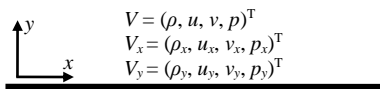


Fig. 13. Schematic of boundary conditions for the MLC schemes on a physical boundary.

For a supersonic inflow boundary, V is specified and imposed. Therefore, V_t and V_x can also be obtained by taking a derivative to t and x . For the subsonic inflow, only a part of the flow quantities is specified. Other quantities can be determined by solving characteristic relations, which is termed the characteristic boundary conditions [99]. The characteristic relation also leads to the equation for V_t . The tangential derivatives V_x can be approximated locally from V along the boundary using high-order finite difference methods like Zhong's compact schemes [21]. Alternatively, we can also derive auxiliary equations for V_x from characteristic relations using the additional degrees of freedom of MLC schemes. For a supersonic outflow boundary, no flow quantities are specified. The boundary conditions are only dependent on information from interior points. They can be obtained by solving Eq. (0.43) using one-sided MLC schemes, or simply extrapolated from interior values. For a subsonic outflow boundary, p is usually specified. Other quantities are determined by solving characteristic relations. The solution procedure is similar to the case in the subsonic inflow. For a solid wall, the non-penetration condition is applied, in other words, (v, v_x, v_t) is 0. Usually, u and p can be determined from interior points by imposing $u_y = 0$ and $p_y = c$, which is a constant determined by the boundary curvature. Characteristic relations can be used to determine other unspecified quantities in V and V_t . The tangential derivatives V_x can be approximated from V by high-order finite difference methods. For all these examples, the normal derivatives V_y can be obtained through Eq. (0.50). It is straightforward to convert (V, V_x, V_y) to (U, U_x, U_y) , and the details are not discussed here.

Navier-Stokes Equations

The Navier-Stokes equations for compressible viscous flows have been introduced in Eq. (0.34). Like the case of the Euler equations, auxiliary equations need to be derived before applying the MLC schemes. Taking gradient on Eq. (0.34), we obtain the auxiliary equations for the Navier-Stokes equations as follows,

$$\frac{\partial U_{x_k}}{\partial t} + \frac{\partial F_{jx_k}}{\partial x_j} + \frac{\partial F_{vjx_k}}{\partial x_j} = 0 \quad (0.51)$$

where the subscripts x_k and j are directional derivatives and dummy index respectively, same as in the Euler equations, and v represents viscous flux term. In vector forms, the original Navier-Stokes equations (0.34) and the auxiliary equations (0.51) can be written as,

$$\frac{\partial}{\partial t} \begin{bmatrix} U \\ U_{x_k} \end{bmatrix} = - \begin{bmatrix} A_j U_{x_j} \\ F_{jx_k x_j} \end{bmatrix} - \begin{bmatrix} F_{vjx_j} \\ F_{vjx_k x_j} \end{bmatrix} \quad (0.52)$$

Note that Eq. (0.52) have the viscous terms on the right-hand side, which is the only difference from Eq. (0.43). Therefore, the treatment of the first term on the right-hand side of Eq. (0.52) follows exactly the same procedures for the Euler equations. In the viscous part, the term $F_{vjx_k x_j}$ also needs an approximation. It can be computed by high-order MLC schemes from F_{vj} and F_{vjx_k} , like the treatment for the inviscid part. However, only the viscous flux F_{vj} can be calculated exactly. The first derivatives F_{vjx_k} needs to be numerically approximated which is explained below. The expression of F_{vj} has been given in Eq. (0.37), and the expression of F_{vjx_k} is derived by taking the derivative of Eq. (0.37) as follows,

$$F_{vjx_k} = \begin{bmatrix} 0 \\ \tau_{1jx_k} \\ \tau_{2jx_k} \\ \tau_{3jx_k} \\ \tau_{ijx_k} u_i + \tau_{ij} u_{ix_k} + q_{jx_k} \end{bmatrix} \quad (0.53)$$

where the subscript i is a dummy index, and the derivatives of viscous stress, molecular viscosity coefficient, and heat flux can be obtained easily as follows,

$$\tau_{ijx_k} = -\mu_{x_k} (u_{ix_j} + u_{jix_i}) - \mu (u_{ix_jx_k} + u_{jix_ix_k}) + \frac{2}{3} (\mu_{x_k} u_{ix_i} + \mu u_{ix_ix_k}) \delta_{ij} \quad (0.54)$$

$$q_{jx_k} = -\kappa T_{x_jx_k} \quad (0.55)$$

The molecular viscosity coefficient μ and its derivative can be calculated by Sutherland's law in the form,

$$\mu = \mu_0 \left(\frac{T}{T_0} \right)^{3/2} \frac{T_0 + T_s}{T + T_s} \quad (0.56)$$

$$\mu_{x_k} = \mu_0 \left(\frac{T}{T_0} \right)^{1/2} \left(\frac{T_0 + T_s}{T + T_s} \right) \left[\frac{3}{2T_0} - \frac{T}{T_0(T + T_s)} \right] T_{x_k} \quad (0.57)$$

Combining Eqs. (0.37) - (0.41) and (0.53) - (0.55), we find that F_{vj} and F_{vjxk} are functions of the primitive variables (u_i, T) and their derivatives in the following form,

$$\begin{aligned} F_{vj} &= f(u_i, T, u_{ix_j}, T_{x_j}) \\ F_{vjx_k} &= f'(u_i, T, u_{ix_j}, T_{x_j}, u_{ix_kx_j}, T_{x_kx_j}) \end{aligned} \quad (0.58)$$

where $i, j, k \in \{1, 2, 3\}$. At every grid point, we know U and U_{xk} from the solution, so u_i, T and their first derivatives can be obtained easily. However, $u_{ix_kx_j}$ and $T_{x_kx_j}$ in Eq. (0.58) needs to be approximated by finite difference methods.

The procedures of discretization for Navier-Stokes equations include three steps. Step 1 is the discretization for inviscid flux. In Step 2, we apply the central MLC schemes to approximate ($u_{ix_kx_j}, T_{x_kx_j}$) from (u_i, T) and their first derivatives. Then using Eq. (0.58), the value of F_{vj} and F_{vjxk} at each point is obtained. In Step 3, we apply the same central MLC schemes to compute F_{vjxkxj} from F_{vj} and F_{vjxk} . After that, all the terms in the right-hand side of Eq. (0.52) is obtained. It should be noted that the central MLC schemes are applied twice in the approximation of viscous terms. To be consistent, the formulas for these central schemes are the same as those for $F_{jx_kx_j}$ in step 1. However, $\alpha = 0$ is always used in the viscous terms due to their elliptic property. After the three steps are finished, Eq. (0.52) becomes a system of ordinary differential equations, which can be solved through the method of lines.

The boundary conditions of U and U_{xk} are needed for the Navier-Stokes simulations. For the inflow and outflow boundaries, the boundary conditions are very similar to those for the Euler equations. This topic is another important area in numerical simulations and the details are not

discussed in this dissertation. However, the solid wall condition for the Navier-Stokes equations is different, because the viscous effect is dominant near the wall. Flow quantities on the solid wall boundaries are $(p, u_i, T, p_x, u_{ix}, T_x, p_y, u_{iy}, T_y)$, where $i = 1, 2, 3$. The subscript x and y represent the tangential and normal direction of the wall, which follows the schematic in Fig. 13. The boundary conditions for ρ can be determined through thermodynamic relations. Specifically, the physical conditions in the Navier-Stokes simulations are: the non-slip condition for u_i , and the isothermal or adiabatic condition for T .

Table 1 summarizes the boundary conditions for the Navier-Stokes simulations with the MLC schemes. According to boundary layer equations, the zero-gradient condition for p can be derived, i.e., p_y on the wall is zero. This condition can usually be extended to the Navier-Stokes simulations. Then, a zero-gradient fitting from the interior points can be used to determine p on the wall. The non-slip boundary condition is applied to $\mathbf{u} = (u_1, u_2, u_3)$. There is no relative motion between the wall and its neighboring fluid particles, i.e., $\mathbf{u} = \mathbf{U}_{\text{wall}}$. If the wall is static, all components u_i are 0. Two types of boundary conditions of T can be used, 1) isothermal wall; 2) adiabatic wall. For isothermal case, T is a constant value; and for the adiabatic case, T_y at the wall is zero which means no heat conduction through the wall. In the adiabatic case, T is determined by the zero-gradient fitting from interior temperatures. The tangential derivatives u_{ix} and T_x in the isothermal case are set to be 0. For p_x and T_x in the adiabatic case, they are approximated by Zhong's compact schemes [21] along the tangential direction of the wall. For u_{iy} and T_y in the isothermal case, the two-layer extrapolation can be used.

Table 1. Summary of boundary conditions for the Navier-Stokes equations.

	Value	Tangential derivative (x)	Normal derivative (y)
p	Zero-gradient fitting	Compact finite difference approximation	Zero
u_i ($\mathbf{u} = \mathbf{U}_{\text{wall}}$)	Non-slip wall	Zero	Two-layer extrapolation
T	1) Isothermal wall ($T = T_{\text{wall}}$)	Zero	Two-layer extrapolation
	2) Adiabatic wall (Zero-gradient fitting)	Compact finite difference approximation	Zero

The two-layer extrapolation and the zero-gradient fitting are very similar, which follows the same multi-layer idea of the MLC schemes. In the following description, we use the T for illustration. The normal derivative is notated as T' for simplicity. For a base point i , the approximation of T' has the form,

$$T'_i = \frac{1}{h} \sum_{l=-L_1}^{L_2} a_l T_{i+l} + \sum_{\substack{m=-M_1 \\ m \neq 0}}^{M_2} b_m T'_{i+m} - \frac{\alpha}{(p+1)!} T_i^{p+1} h^p + \dots \quad (0.59)$$

where all the coefficients are defined in the same way as in Eq. (0.4). These two formulas are very similar, both include two layers of information – value and first derivatives. However, the second derivative in Eq. (0.4) is replaced by the first derivative in Eq. (0.59). As a result, this approximation of T'_i can be considered as a combination of the interpolation/extrapolation from T'_{i+m} and the finite difference approximation from T_{i+l} . The coefficients a_l and b_m can be derived from the Taylor series expansion. On a boundary point ($i = 1$), one-sided stencils are used ($L_1 = M_1 = 0$), then the formulas for the two-layer extrapolation are obtained, as follows,

$$T'_1 = \frac{1}{h} \sum_{l=0}^{L_2} a_l T_{1+l} + \sum_{m=1}^{M_2} b_m T'_{m+1} \quad (0.60)$$

For the isothermal wall, all values at the right-hand side of Eq. (0.60) are known, therefore, T'_1 on the wall can be computed. By using the first derivatives in the inner field which are already solved, the two-layer extrapolation achieved the same accuracy with fewer points compared with finite difference approximations or conventional extrapolation of normal derivatives. Hence, it is more compatible with the MLC schemes.

In the adiabatic case, T'_1 on the wall is zero, and T_1 is the unknown. With some algebraic operations, Eq. (0.60) can be written in the following form,

$$T_1 = -\frac{1}{a_0} \left(\sum_{l=1}^{L_2} a_l T_{1+l} + h \sum_{m=1}^{M_2} b_m T'_{m+1} \right) \quad (0.61)$$

where all the coefficients keep the same values from Eq. (0.60). The approximation in Eq. (0.61) is termed the zero-gradient fitting, which also applies to the approximation of boundary pressures.

4.7 Fourier Analysis

In this section, the one-dimensional and two-dimensional Fourier analysis is performed respectively on various MLC schemes. The dissipative and dispersive errors, spectral resolution, and anisotropic error are analyzed and compared.

One-Dimensional Fourier Analysis

The dissipative and dispersive errors of the upwind MLC schemes applied to advection equation (0.3) are investigated by the Fourier analysis. The trial solutions in Fourier mode are of the following form,

$$\begin{bmatrix} u \\ u' \end{bmatrix} = \begin{bmatrix} \hat{u} \\ \hat{u}' \end{bmatrix} e^{\hat{a}t + i\hat{k}x} \quad (0.62)$$

where

\hat{k} is the wavenumber, and \hat{a} is a complex characteristic parameter as a function of \hat{k} . If a uniform mesh with spacing h is used, the Fourier modes can also be written in discrete form as,

$$\begin{bmatrix} u_i \\ u'_i \end{bmatrix} = \begin{bmatrix} \hat{u} \\ \hat{u}' \end{bmatrix} e^{\hat{a}t + i\hat{k}x_i} \quad (0.63)$$

where $x_i = x_0 + ih$. The temporal derivative is assumed to be exact and does not introduce any error. Using the L_1 - L_2 - M_1 - M_2 scheme given by Eq. (0.4) with the stencil in Fig. 3 to discretize the spatial derivative u'' , the advection equation (0.3) becomes two semi-discrete equations as follows,

$$\frac{d}{dt}u_i + cu'_i = 0 \quad (0.64)$$

$$\frac{d}{dt}u'_i + \frac{c}{h} \left(\frac{1}{h} \sum_{l=-L_1}^{L_2} a_l u_{i+l} + \sum_{m=-M_1}^{M_2} b_m u'_{i+m} \right) = 0 \quad (0.65)$$

where u_{i+l} and u'_{i+m} can be represented in discrete Fourier modes according to Eq. (0.63) in this analysis,

$$u_{i+l} = \hat{u} e^{\hat{a}t + i\hat{k}(x_i + lh)} \quad (0.66)$$

$$u'_{i+m} = \hat{u}' e^{\hat{a}t + i\hat{k}(x_i + mh)} \quad (0.67)$$

Substituting Eqs. (0.66) and (0.67) into Eq. (0.64) leads to the following relation between \hat{u} and \hat{u}' ,

$$\hat{u}' = -\frac{\hat{a}}{c} \hat{u} \quad (0.68)$$

Then, substituting Eqs. (0.66) and (0.67) into Eq. (0.65) and using the relation in Eq. (0.68) results in a quadratic characteristic equation for a ,

$$a^2 + Ba + C = 0 \quad (0.69)$$

where a is the non-dimensional dissipation factor defined as,

$$a = R\left(\frac{\hat{a}h}{c}\right) - i \cdot I\left(\frac{\hat{a}h}{c}\right) \quad (0.70)$$

Operators R and I represent taking real and imaginary parts respectively, and B and C are complex constants dependent on the specific choice of the MLC schemes and wavenumber \hat{k} , as given below,

$$B = \sum_{m=-M_1}^{M_2} b_m e^{-imh\hat{k}}, \quad C = -\sum_{l=-L_1}^{L_2} a_l e^{-ilh\hat{k}} \quad (0.71)$$

Equation (0.69) has two complex solutions,

$$a_{1,2} = \frac{-B \pm \sqrt{B^2 - 4C}}{2} \quad (0.72)$$

where one is the physical mode, and the other is spurious mode. The real part $R(a)$ is a dissipation factor which is related to stability and dissipative error, and the imaginary part $I(a)$ is the modified wavenumber and it can reveal the dispersive error. Meanwhile, the exact solution of a can be derived by substituting Eq. (0.62) into Eq. (0.3),

$$a_{exc} = i\hat{k}h = ik \quad (0.73)$$

where k is the non-dimensional wavenumber. Since there are two solutions of a for the new MLC scheme, we use a_1 to represent the physical mode, and a_2 to represent the spurious mode. The physical mode a_1 should be as close as possible to a_{exc} for better accuracy. From the following formula,

$$a_1 - a_{exc} = R(a_1) + i(I(a_1) - k) \quad (0.74)$$

it is required that $R(a_1)$ is small to reduce dissipative error, and $I(a_1)$ is close to k for small dispersive error. On the other hand, $R(a_1)$ and $R(a_2)$ should be non-positive to ensure the stability of the MLC scheme. Meanwhile, $R(a_2)$ is related to the stiffness of the MLC scheme. If its magnitude is too large, the numerical problem will be too stiff.

Before we present the Fourier analysis results for MLC schemes, the benefit of introducing the derivative layer can be briefly explained through aliasing in the discrete domain. At an arbitrary time, the Fourier mode sampled at the grid point x_i can be represented as,

$$u_i = \hat{u} e^{i(kn + \varphi)} = \hat{u} [\cos(kn + \varphi) + i \sin(kn + \varphi)] \quad (0.75)$$

where n is the index of grid point x_i , and φ is a time-dependent real number. Without the derivative layer, the Fourier mode with a different wavenumber

$$k_{alias} = k + 2N\pi \quad (0.76)$$

can produce the same samples, where N can be any integer. When the mode is reconstructed from these samples, the reconstructed wavenumber k_{rec} is the k_{alias} with the smallest magnitude. As a result, only the k in $[-\pi, \pi]$ can be corrected reconstructed from the sample values. Specifically, the following relation can be obtained,

$$k_{rec} = \begin{cases} k, & k \in (0, \pi] \\ k - 2\pi, & k \in (\pi, 2\pi] \end{cases} \quad (0.77)$$

Therefore, the wave components with $k > \pi$ cannot be resolved by a mono-layer scheme like conventional finite difference methods, because these waves cannot be represented correctly in the discrete domain. The aliasing is the main reason limiting the marginal resolution of finite difference methods. However, with the introducing of the derivative layer in our MLC schemes, another sample is generated at the grid point x_i ,

$$u'_i = k \hat{u} e^{i(kn + \varphi + \pi/2)} / h = k \hat{u} [-\sin(kn + \varphi) + i \cos(kn + \varphi)] / h \quad (0.78)$$

Because the magnitude of derivatives is dependent on k , Fourier modes with different k 's cannot generate the same samples. In another word, the aliasing is avoided. Therefore, the small waves with large k 's can also be represented correctly in the discrete domain, which makes it possible to resolve them with the MLC schemes. More discussion about the spectral resolution is presented in the Fourier analysis results.

Fourier Analysis of the Seventh-Order 2-2-2-2 Scheme

In the first place, the seventh-order 2-2-2-2 scheme is analyzed using the approach presented above. Fig. 14 presents the Fourier analysis results for the 2-2-2-2 scheme with a typical α value of 12, where the results of Zhong's sixth-order and fifth-order compact scheme with $\alpha = 0$ and -1, and Zhong's fifth-order explicit scheme with $\alpha = -6$ [21] are also presented for comparison. Here, only

physical mode a_1 is plotted for the MLC scheme. Fig. 14(a) shows that all these schemes are stable with non-positive dissipation factors. Zhong's sixth-order central scheme with $\alpha = 0$ has no dissipation and coincides with the exact solution. With upwind setting, all schemes become dissipative for large k . Compared with Zhong's explicit scheme, Zhong's compact scheme has smaller dissipation when $k < 2.4$, however, the dissipation grows rapidly and surpass explicit scheme for large k . Both schemes have the largest dissipation when $k = \pi$. On the other hand, the 2-2-2-2 scheme is much less dissipative in all the plotted k range compared with Zhong's compact and explicit schemes, which indicates a better accuracy as well.

Fig. 14(b) compares the modified wavenumbers of these schemes, where the straight line represents the exact wavenumber. As expected, Zhong's compact schemes with two different α values have a better resolution than Zhong's explicit scheme. However, the accuracies of these 3 schemes decrease rapidly as k increases and drop to zero at $k = \pi$, which is the maximum resolution that most explicit and compact finite difference scheme can achieve in theory. On the other hand, the 2-2-2-2 scheme shows a very high resolution for $k > \pi$, which is similar to the resolution of spectral methods. That means the MLC scheme is much more accurate for resolving flow with very small wavelengths. In other words, it can compute the wave solutions accurately with much fewer grid points per period. This advantage in the resolution of the new MLC schemes is due to additional degrees of freedom contained in each grid point, i.e., both the point value and its first derivative. It should be noted that both the seventh-order 2-2-2-2 scheme and Zhong's fifth-order explicit scheme use the explicit formula, but the former is constructed on a five-point grid stencil while the latter needs a seven-point stencil. In other words, the resolution of the 2-2-2-2 scheme is much better on a shorter stencil, which validates the idea that the MLC scheme can reach very high-order accuracy and spectral-like resolution within a compact stencil.

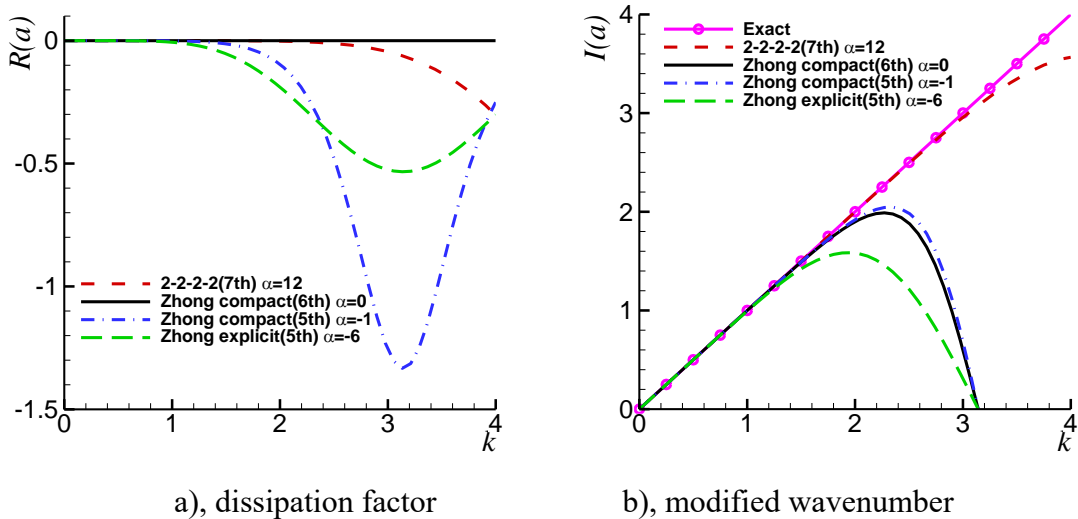


Fig. 14. Fourier analysis results of the 2-2-2-2 scheme (7th order), in comparison with Zhong's compact scheme (5th and 6th order) and Zhong's explicit scheme (5th order) [21].

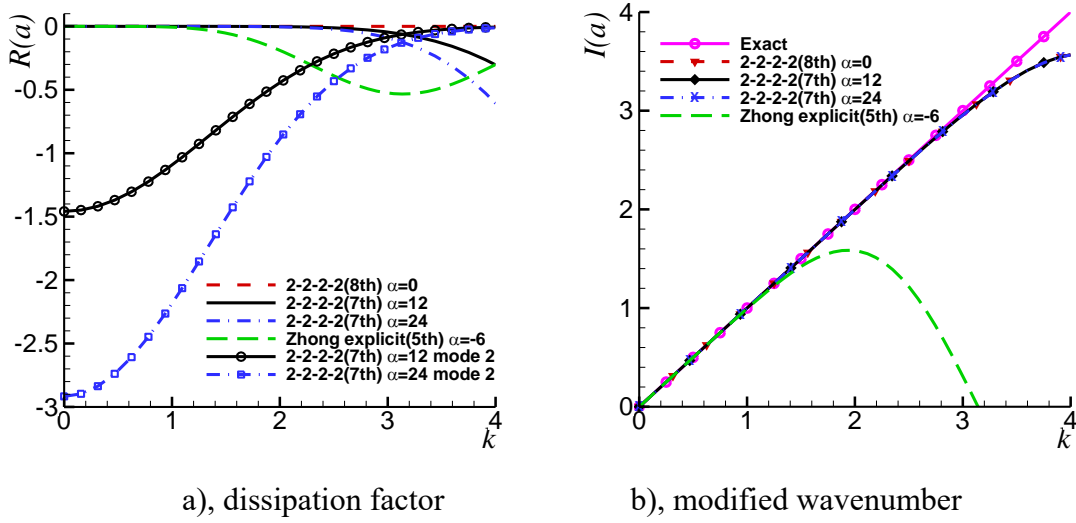


Fig. 15. Fourier analysis results of the 2-2-2-2 scheme (7th order) with different upwind coefficients.

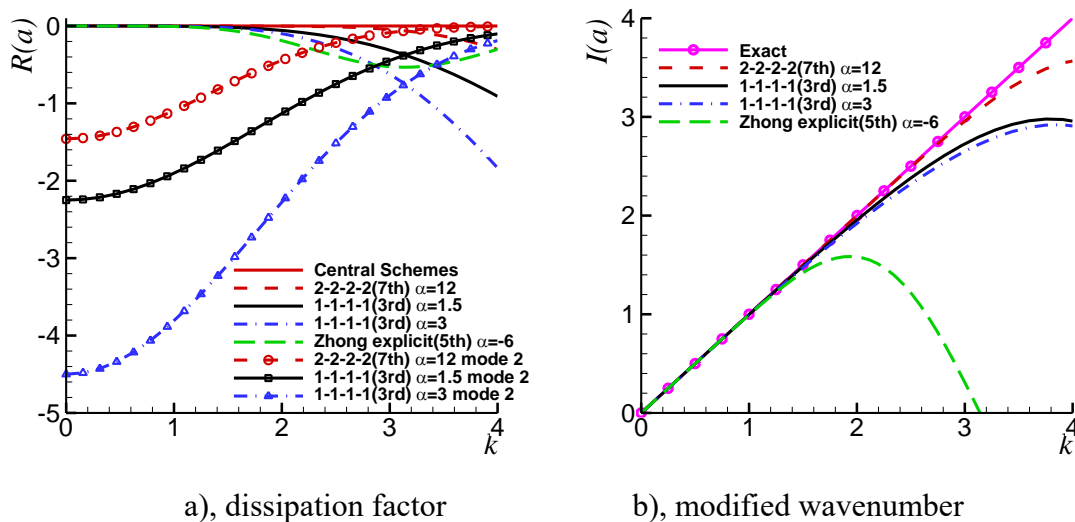
The effect of different α values on the accuracy of the 2-2-2-2 scheme are presented. The choice of α has an impact on dissipation, dispersion, and stiffness of the numerical schemes. Fig. 15 presents the Fourier analysis results for three different 2-2-2-2 schemes with $\alpha = 0, 12, 24$, where the result of Zhong's fifth-order explicit scheme with $\alpha = -6$ is presented for comparison. To analyze the effect of α on stiffness, the dissipation factor of spurious mode $-R(a_2)$ of the 2-2-2-2 scheme is also presented. Different from $R(a_1)$, which are consistent with exact solution for small k and deviate for large k , $R(a_2)$ show large dissipation for small k . This behavior benefits the accuracy of the scheme because the spurious wave will damp out in the simulation when grid resolution is good enough. Another important information revealed by $R(a_2)$ is the restriction on the time step size in the temporal discretization or termed the stiffness of the scheme. It is well known from the numerical analysis theory that $|\hat{a}\Delta t|$ should fall into the stability region of time integration scheme if the resulting ordinary differential equation is discretized by explicit methods such as Runge-Kutta methods. Since $R(a_2)$ is much larger than $R(a_1)$, $I(a_1)$, and $I(a_2)$ in magnitude when k is small, the stiffness of the scheme is mainly determined by $R(a_2)$. A larger magnitude of $R(a_2)$ indicates a smaller time step size Δt under the same stability condition, i.e., the integral of the resulting ordinary differential equation is more restrictive in terms of choosing time step size. Fig. 15 (a) shows that larger upwind coefficient α makes $R(a_2)$ much more dissipative for small k , which should result in more restrictive time step size. In addition, larger α also make $R(a_1)$ more dissipative for large k , which can affect the accuracy when small length wave is important in the flow.

On the other hand, Fig. 15 (b) shows that 2-2-2-2 schemes with different upwind coefficients have similar resolutions in terms of wavenumber. All of them are much better than Zhong's fifth-order explicit scheme. In summary, α should be large enough to ensure stability, but not too large to avoid stiffness and keep small dissipation. For seventh-order 2-2-2-2 scheme, $\alpha = 12$ is recommended, although other values of α could also be considered.

Fourier Analysis of the Third-Order 1-1-1-1 Scheme

In the next place, the third-order 1-1-1-1 scheme is analyzed and the impact of different values of α is discussed. Fig. 16 presents the Fourier analysis results of two different 1-1-1-1 schemes with $\alpha = 1.5$ and 3, where results of the seventh-order 2-2-2-2 scheme with $\alpha = 12$ and Zhong's fifth-order explicit scheme with $\alpha = -6$ are also presented for comparison. Same as Fig. 15, dissipation factors of both physical and spurious modes $-R(a_1)$ and $R(a_2)$ are plotted to show dissipation and stiffness of the 1-1-1-1 scheme, and modified wavenumber of spurious mode $-I(a_1)$ is plotted to show resolution. Fig. 16 (a) shows that the 1-1-1-1 schemes with both α values have larger dissipation factors than the 2-2-2-2 scheme, as well as errors in modified wavenumber showed in Fig. 16 (b). This is reasonable that high-order MLC scheme is more accurate than low-order MLC scheme considering both dissipative and dispersive errors. Furthermore, Fig. 16 (b) indicates the third-order 1-1-1-1 scheme has a much better resolution for large k than Zhong's fifth-order explicit scheme though the former is two orders lower than the latter. This advantage can be explained by the additional degrees of freedom contained on each grid points. In addition, Fig. 16 (a) shows that the 1-1-1-1 scheme has smaller dissipation than Zhong's explicit scheme for a wide range of k as well. Specifically, the 1-1-1-1 scheme with $\alpha = 3$ are less dissipative than Zhong's fifth-order explicit scheme when $k < 2.8$; and the 1-1-1-1 scheme with $\alpha = 1.5$ are less dissipative than Zhong's fifth-order explicit scheme when $k < 3.4$, which covers the entire significant range $[0, \pi]$ of conventional finite difference scheme.

Increasing upwind coefficients α introduces more dissipation for both $R(a_1)$ and $R(a_2)$ as Fig. 16 (a) shows. Meanwhile, increasing α also decreases the resolving ability slightly as observed in Fig. 16 (b). So, larger α makes the 1-1-1-1 scheme less accurate. Similar to the discussion for the 2-2-2-2 scheme, the magnitude of $R(a_2)$ affects the stiffness of the problem, which indicates an increase of α leads to increase of stiffness. On the other hand, α should be large enough to ensure stability. Considering stability, accuracy, and stiffness, the recommended value for α is 1.5 for third-order 1-1-1-1 scheme. Again, other values could also be considered.



a), dissipation factor
b), modified wavenumber
Fig. 16. Fourier analysis results of the 1-1-1-1 scheme (3rd order) with different upwind coefficients.

Fourier Analysis of MLC Schemes on Bias Stencils

MLC schemes with bias grid stencils including the 2-1-2-1, 2-1-1-1 and 1-1-2-1 schemes are also analyzed using Fourier analysis approach. These MLC schemes follow traditional upwind schemes, where the bias stencil introduces enough numerical dissipation to control the aliasing errors and to enhance the numerical stability [21]. On the other hand, the upwind MLC schemes follow Zhong’s upwind compact and explicit scheme [21] by using the centered stencil with an adjustable parameter α in the leading dissipative truncation term. Fig. 17 compares the Fourier analysis results of the sixth-order 2-1-2-1 scheme, the fifth-order 2-1-1-1 scheme, and the fifth-order 1-1-2-1 scheme on bias stencils, where the seventh-order 2-2-2-2 scheme on the centered stencil with $\alpha = 12$ is also presented for comparison. Only physical mode a_1 is plotted to compare accuracies. Fig. 17 (b) shows that all the schemes have a spectral-like resolution. Specifically, the seventh-order 2-2-2-2 scheme on centered stencil has better resolution than the fifth-order 2-1-1-1 and 1-1-2-1 schemes on bias stencils, but worse than the sixth-order 2-1-2-1 scheme on bias stencil. However, Fig. 17 (a) shows the 2-1-2-1 scheme has the largest dissipation among all schemes while the 2-2-2-2 scheme has the smallest dissipation. Overall, the upwind 2-2-2-2 scheme is more favorable, because it has the smallest dissipation and very good spectral resolution, although lower than the resolution of the 2-1-2-1 scheme for large k . This observation is consistent with the conclusion in [21] that upwind scheme on centered grid stencil have smaller dissipation than those on upwind-bias grid stencil. As for the comparison of fifth-order 2-1-1-1 scheme which has bias stencil on the value layer, and fifth-order 1-1-2-1 scheme which has bias stencil on the derivative layer, there is no much difference except the latter is slightly more dispersive and less dissipative. Therefore, using bias stencil on value layer introduces slightly larger dissipation than the bias setting for the derivative layer.

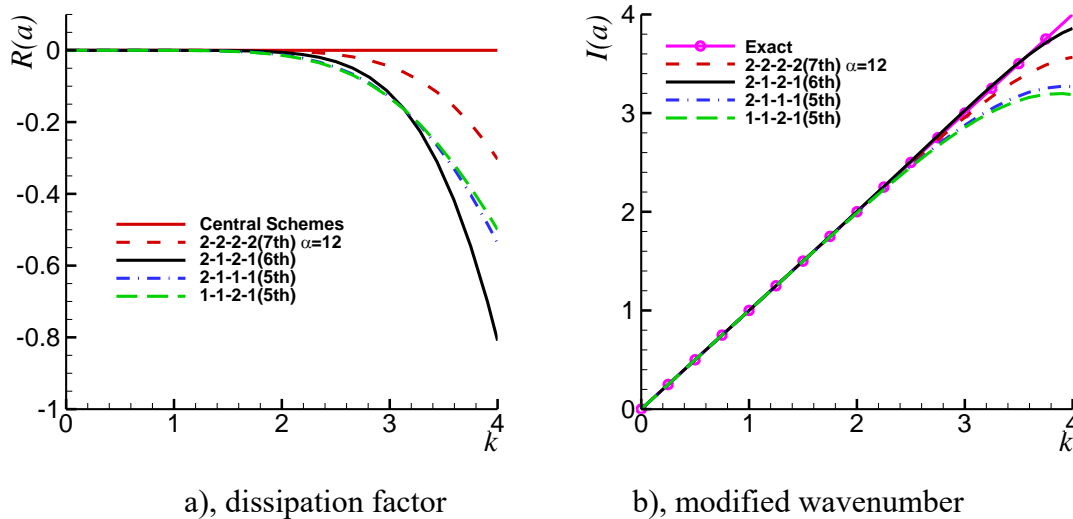


Fig. 17. Comparison of the MLC schemes on the centered and bias stencils.

Fig. 18 presents $R(a_1)$ and $R(a_2)$ together for the three MLC schemes on bias stencils to compare the stiffness of these different MLC schemes. The 2-1-2-1 scheme which uses bias stencil on both value and derivative layers have the largest dissipation in $R(a_1)$ and $R(a_2)$; the 2-1-1-1 scheme which

uses bias stencil on the value layer has slightly larger dissipation than the 1-2-1-1 scheme which uses bias stencil on the derivative layer. Therefore, using bias stencil introduces larger dissipation in both $R(a_1)$ and $R(a_2)$, and its effect is more obvious when applied to the value layer. In addition, using bias stencil on both the value and derivative layer may introduce too much dissipation in $R(a_2)$. For example, the maximum magnitude of $R(a_2)$ is about 3.9 for 2-1-2-1 scheme. As comparison, the maximum is about 1.5 for the 2-2-2-2 scheme with $\alpha = 12$ in Fig. 15 (a), and it is about 2.2 for 1-1-1-1 scheme with $\alpha = 1.5$ in Fig. 16 (a). As a result, the 2-1-2-1 scheme requires smaller time step size in temporal discretization. From the above analysis, it is more appropriate to construct upwind MLC schemes on centered stencils considering stability, dissipation, and stiffness. In fact, the 2-1-1-1 and 1-1-2-1 schemes can be considered as special cases on centered stencils with some large values of α .

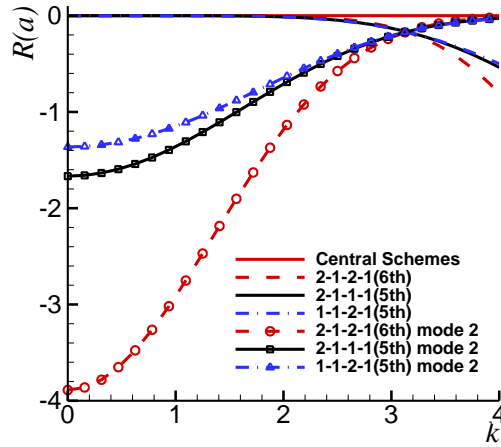


Fig. 18. Dissipation factors of physical and spurious modes of the MLC schemes on bias stencils.

Fourier Analysis of Pure Upwind MLC Schemes

In conventional finite difference methods, stable upwind schemes can be derived on one-sided bias stencils. For example, a second-order upwind scheme

$$u'_i = \frac{1}{2h}(u_{i-2} - 4u_{i-1} + 3u_i) \quad (0.79)$$

can be derived by using two points on the upwind side. However, the fourth-order 2-0-2-0 scheme constructed on the similar stencil is unstable. Fig. 19 shows the Fourier analysis results of the 2-0-2-0 scheme and other unstable pure upwind MLC schemes, where the results of the seventh-order 2-2-2-2 scheme with $\alpha = 12$ is also presented for comparison. Here, only physical mode a_1 is plotted for the MLC schemes. Fig. 19 (a) shows that the MLC schemes on one-sided bias stencils has positive $R(a_1)$'s which indicate instability of these schemes. The numerical instability increases with the rising order of accuracy. Fig. 19 (b) shows their modified wavenumber $I(a_1)$'s fall on the other side of the exact solution for large k 's, which is different from the 2-2-2-2 scheme. The spectral resolution of the pure upwind MLC schemes are also not as good as the 2-2-2-2 scheme.

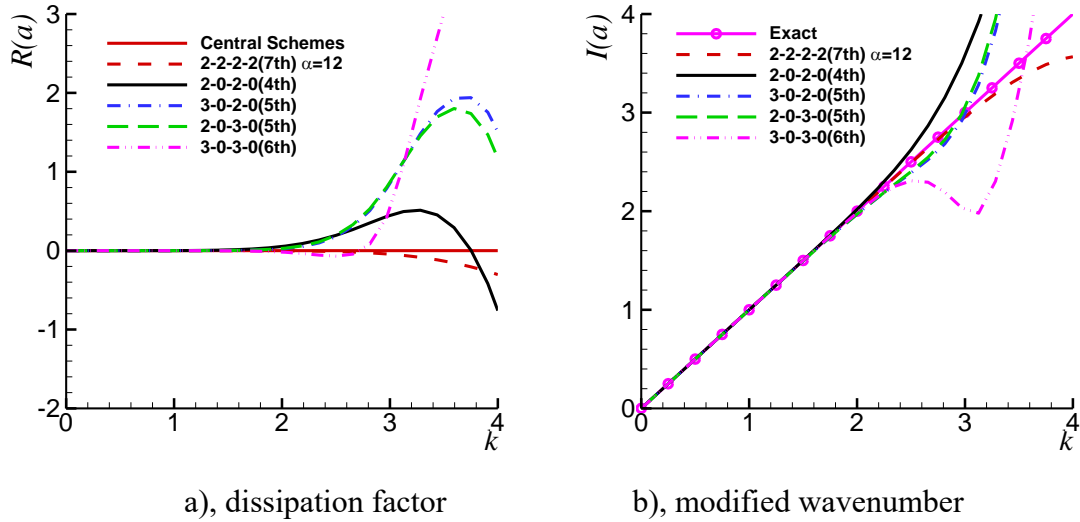
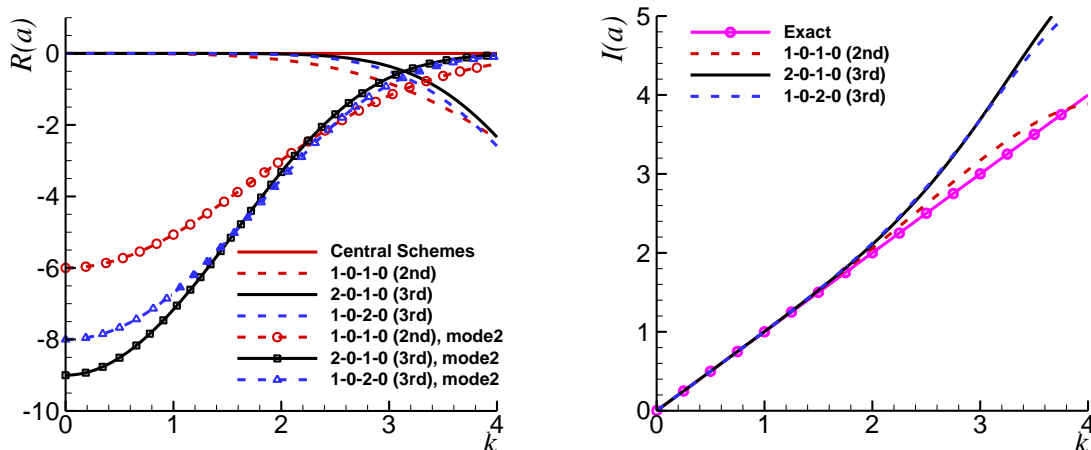


Fig. 19. Fourier analysis results of the unstable MLC schemes on one-sided bias stencils.

The instability of the pure upwind MLC schemes is unexpected because one-sided stencils usually leads to stable schemes in conventional finite difference methods. However, the MLC scheme introduces additional degrees of freedom which makes numerical stability more complicated. It is discovered through further Fourier analysis that the stability of the pure upwind MLC scheme is affected by the imbalance level of the stencils. Fig. 20 (a) shows that the 1-0-1-0, 2-0-1-0, and 1-0-2-0 schemes are stable, which have less imbalance than the 2-0-2-0 scheme or other pure upwind schemes in Fig. 19. However, the $R(a_2)$ of these pure upwind MLC schemes show much larger dissipations for small k 's compared with previous examples (see Fig. 15, Fig. 16, Fig. 18), which should result in more restrictive time step sizes. Fig. 20 (b) shows that their dispersive error is also larger, and the spectral resolution reduces with the increasing imbalance level. On the other hand, any pure upwind MLC scheme with fourth or higher order of accuracy are proven to be unstable through Fourier analysis, as shown in Fig. 19. Therefore, the stability and accuracy of pure MLC scheme are very sensitive to the imbalance level of stencils, and very high-order MLC scheme cannot be derived on one-sided bias stencils.



a), dissipation factor

b), modified wavenumber

Fig. 20. Fourier analysis results of the stable MLC schemes on one-sided bias stencils.

In summary, the one-dimensional Fourier analysis in this section shows that: 1) the stable MLC scheme can be constructed on centered stencils with upwind coefficients α , or on upwind bias stencils; 2) it has very high resolution, small dissipative and dispersive errors, reasonable stiffness. Comparison of the 1-1-1-1 scheme and Zhong's fifth-order explicit scheme indicates even lower order MLC scheme can have better resolution and smaller dissipation than conventional higher-order scheme; 3) the value of α has an impact on the stability, accuracy, and stiffness of the MLC scheme. The recommended value of α is 12 for the seventh-order 2-2-2-2 scheme and 1.5 for the third-order 1-1-1-1 scheme; 4) using upwind bias stencils for MLC schemes introduces larger dissipation than using a centered stencil and adjustable parameter α , and pure upwind MLC schemes with fourth or higher order of accuracy are unstable.

Two-Dimensional Fourier Analysis

The dissipation and dispersive errors of the upwind MLC schemes applied to two-dimensional advection equation (0.28) are also investigated by the Fourier analysis. For multi-dimensional simulations, the approximation of the cross derivative terms given in Eq. (0.29) could lead to different stability and dissipative properties of the numerical scheme from the one-dimensional analysis. The discretization is based on Cartesian coordinates here. To be generic, the convection angle θ and Fourier wave angle φ are defined in the Fourier analysis. The governing equations are the same as Eq. (0.28), where the dimensional wave speed can be written as,

$$\begin{aligned} c_1 &= c \cdot \cos \theta \\ c_2 &= c \cdot \sin \theta \end{aligned} \quad (0.80)$$

which are functions of convection angle θ and the magnitude of wave speed c . Fourier analysis is carried out by assuming the solution in the following form,

$$\begin{bmatrix} u \\ u_x \\ u_y \end{bmatrix} = \begin{bmatrix} \hat{u} \\ \hat{u}_x \\ \hat{u}_y \end{bmatrix} e^{\hat{a}t + i\hat{k}(x\cos\varphi + y\sin\varphi)} \quad (0.81)$$

where φ is an arbitrary Fourier wave angle, the definitions of \hat{k} and \hat{a} are the same as one-dimensional analysis. The procedure of the two-dimensional Fourier analysis follows the same methodology as in one-dimensional analysis. Substituting the trial solution above into Eq. (0.28), a relation between \hat{u} , \hat{u}_x and \hat{u}_y can be obtained as,

$$\hat{u} = -\frac{c}{\hat{a}}(\hat{u}_x \cos \theta + \hat{u}_y \sin \theta) \quad (0.82)$$

Applying the approximations of second and cross derivatives in Eqs. (0.9) and (0.29), a cubic characteristic equation of the non-dimensional dissipation factor a defined in Eq. (0.70) can be derived,

$$a^3 + Ba^2 + Ca + D = 0 \quad (0.83)$$

Same as one-dimensional analysis, B , C , and D are complex constants dependent on the choice of the finite difference formulas and wavenumber \hat{k} . Meanwhile, they are also functions of θ and φ in two-dimensional analysis as given below,

$$\begin{aligned}
B &= (B_2 + B_3) \sin \theta + (B_1 + C_3) \cos \theta \\
C &= (B_2 B_3 - A_2) \sin^2 \theta + (B_1 C_3 - A_1) \cos^2 \theta + \left(\frac{1}{2} B_1 B_2 - A_3 \right) \sin 2\theta \\
D &= [A_2 (C_3 - B_1) - B_2 A_3] \sin^2 \theta \cos \theta - A_2 B_3 \sin^3 \theta \\
&\quad + [A_1 (B_3 - B_2) - B_1 A_3] \sin \theta \cos^2 \theta - A_1 C_3 \cos^3 \theta
\end{aligned} \tag{0.84}$$

and

$$\begin{aligned}
A_1 &= \sum_{l=-L_1}^{L_2} a_l e^{i h \hat{k} \cos \varphi}, & A_2 &= \sum_{l=-L_1}^{L_2} a_l e^{i h \hat{k} \sin \varphi} \\
B_1 &= \sum_{m=-M_1}^{M_2} b_m e^{i m h \hat{k} \cos \varphi}, & B_2 &= \sum_{m=-M_1}^{M_2} b_m e^{i m h \hat{k} \sin \varphi} \\
A_3 &= \sum_{\substack{l_x=-L_1 \\ l_y=-L_1}}^{L_2} a_{l_x, l_y} e^{i h \hat{k} (l_x \cos \varphi + l_y \sin \varphi)} \\
B_3 &= \sum_{\substack{m_x=-M_1 \\ m_y=-M_1}}^{M_2} b_{m_x, m_y} e^{i h \hat{k} (m_x \cos \varphi + m_y \sin \varphi)} \\
C_3 &= \sum_{\substack{n_x=-M_1 \\ n_y=-M_1}}^{M_2} c_{n_x, n_y} e^{i h \hat{k} (n_x \cos \varphi + n_y \sin \varphi)}
\end{aligned} \tag{0.85}$$

Three roots of Eq. (0.83) correspond to one physical mode a_1 and two spurious modes a_2 , a_3 . The real and imaginary part of a plays the same role as in one-dimensional analysis. The exact solution of a is,

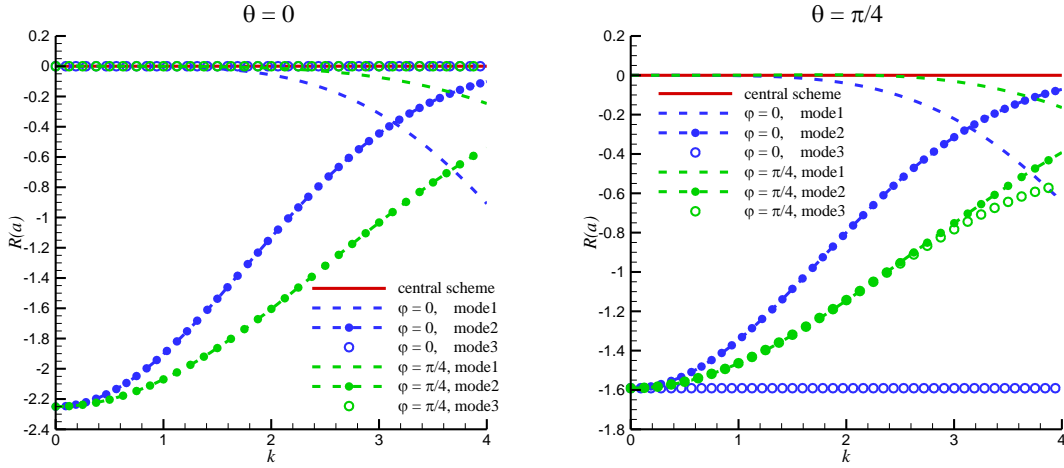
$$a_{exc} = i \hat{k} h \cos(\theta - \varphi) = i k \cos(\theta - \varphi) \tag{0.86}$$

which is a product of one-dimensional exact solution in Eq. (0.73) and a cosine function of θ and φ .

In the two-dimensional Fourier analysis as well as two-dimensional numerical simulations presented later, the one-dimensional MLC schemes with recommended α values are used for the approximation of second derivatives, while cross derivatives are discretized by the two-dimensional MLC schemes with one order higher of accuracy than the one-dimensional scheme. Therefore, the overall accuracy depends on one-dimensional MLC schemes. Different θ and φ are considered in the two-dimensional Fourier analysis.

The two-dimensional Fourier analysis is first carried out to the third-order 1-1-1-1 scheme with $\alpha = 1.5$ as given in Eqs. (0.8) and (0.30). Fig. 21(a) presents the dissipation factors for the case of $\theta = 0$, and Fig. 21(b) shows results for the case of $\theta = \pi/4$. For each case of θ , two cases of φ are compared which also have the values of 0 and $\pi/4$. All three modes are presented, where a_1 is the physical mode and a_2 , a_3 are two spurious modes. The figure shows a_1 and a_2 behave similarly as those of one-dimensional Fourier analysis, while a_3 is the distinctive mode for two-dimensional

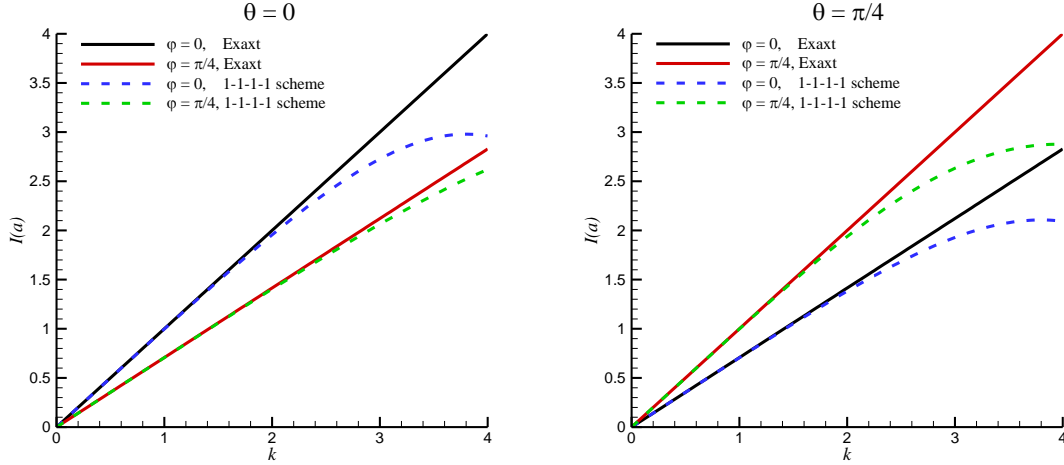
Fourier analysis. When both θ and φ are 0, the results are the same with one-dimensional Fourier results in Fig. 16. The value of $R(a_3)$ depends on both θ and φ . When θ is zero, it is always zero which means spurious mode will keep its initial condition during the simulation. When θ is not zero but φ is zero, $R(a_3)$ is a negative constant which means the spurious mode will be evenly decayed for all the wavenumbers. When both θ and φ is not zero, a_3 behaviors similarly to a_2 . Overall, all three modes are stable in two-dimensional Fourier analysis. Similar to one-dimensional analysis, stiffness is dominated by spurious modes.



a), wave propagation in direction of $\theta = 0$ b), wave propagation in direction of $\theta = \pi/4$

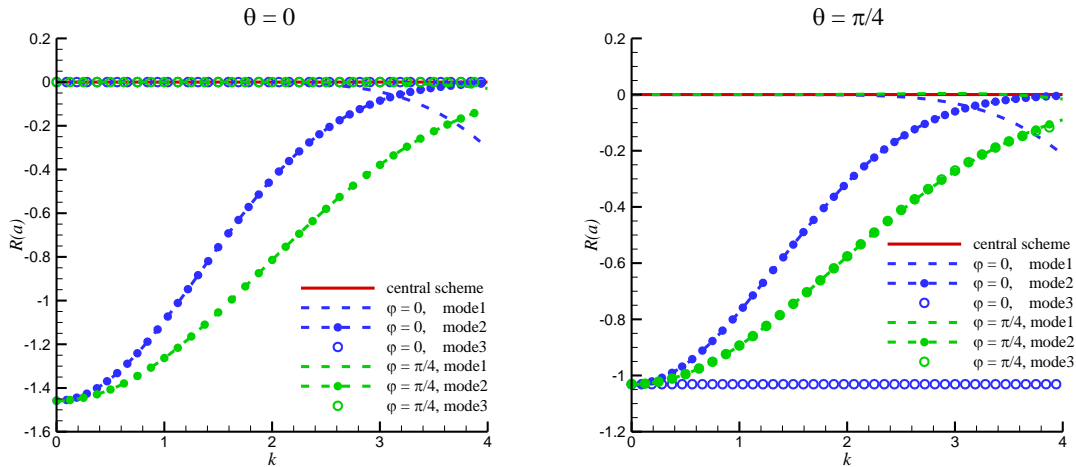
Fig. 21. Dissipation factor $R(a_1)$, $R(a_2)$, $R(a_3)$ of the 1-1-1 scheme (3rd order) for two-dimensional wave propagation.

The modified wavenumber of physical mode $I(a_1)$ for the same 1-1-1 scheme is shown in Fig. 22. It should be mentioned that the spurious modes a_2 and a_3 do not affect accuracy significantly. Even though they affect the stiffness of the problem, the amplitudes of $R(a_2)$, $R(a_3)$ are much larger than those of $I(a_2)$, $I(a_3)$. Therefore, only $I(a_1)$ is plotted in two-dimensional Fourier analysis. In the figures, all the results with different combinations of θ and φ show a good resolution of the scheme for small k . When θ is zero as shown in Fig. 22 (a), the scheme has the best resolution. Comparing the results of (a) and (b), we can observe that the accuracy is reduced when $\theta = \pi/4$. In fact, it is true for all non-zero θ , and this property is well known as the anisotropic error of finite difference methods for multi-dimensional simulations. However, Fig. 22 indicates that the difference is relatively small for the MLC scheme. This favorable property is probably because our MLC schemes take information from neighboring points in all different orientations in the approximation of cross derivatives³. On the other hand, changing of φ does not have an obvious effect on the spectral resolution.

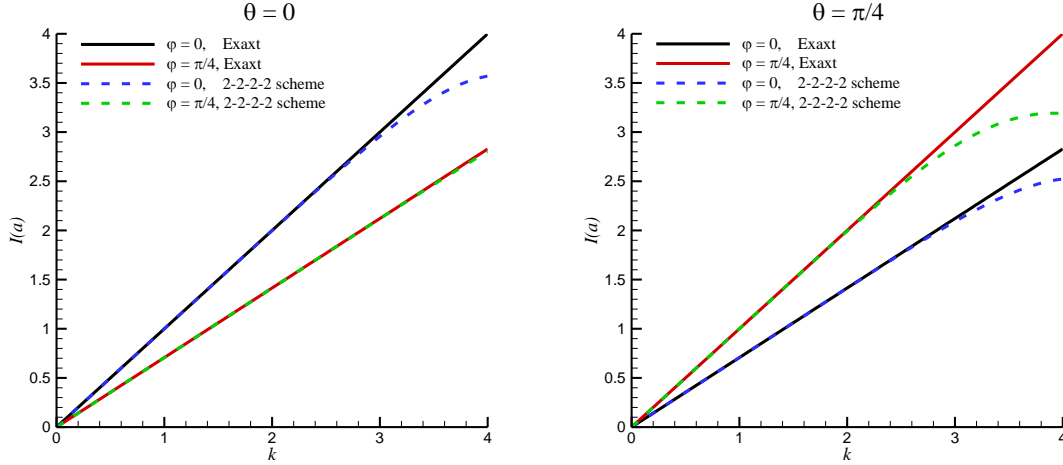


a), wave propagation in direction of $\theta = 0$ b), wave propagation in direction of $\theta = \pi/4$
 Fig. 22. Modified wavenumber $I(a_1)$ of the 1-1-1-1 scheme (3rd order) for two-dimensional wave propagation.

The two-dimensional Fourier analysis is then carried out to the seventh-order 2-2-2-2 scheme with $\alpha = 12$ as given in Eqs. (0.11) and (0.31). Dissipation factors of all three modes are presented in Fig. 23, and modified wavenumber of physical mode a_1 is shown in Fig. 24. Comparing Fig. 21 and Fig. 23, we observe that all modes of the 2-2-2-2 scheme are less dissipative than those of 1-1-1-1 scheme. Comparing Fig. 22 and Fig. 24, we can see the resolution of the 2-2-2-2 scheme for large k is better than that of the 1-1-1-1 scheme. Both aspects indicate 2-2-2-2 scheme is much more accurate than the 1-1-1-1 scheme in two-dimensional simulations. In addition, similar effects of θ and φ on the resolution as 1-1-1-1 scheme can be observed in the results of the 2-2-2-2 scheme which indicates the anisotropic error is still very small.



a), wave propagation in direction of $\theta = 0$ b), wave propagation in direction of $\theta = \pi/4$
 Fig. 23. Dissipation factor $R(a_1)$, $R(a_2)$, $R(a_3)$ of the 2-2-2-2 scheme (7th order) for two-dimensional wave propagation.



a), wave propagation in direction of $\theta = 0$ b), wave propagation in direction of $\theta = \pi/4$
 Fig. 24. Modified wavenumber $I(a_1)$ of the 2-2-2-2 scheme (7th order) for two-dimensional wave propagation.

4.8 Summary of the New MLC Schemes

In this section, our new very high-order upwind MLC scheme has been presented and analyzed by Fourier analysis and stability analysis with matrix methods. The aliasing in conventional finite difference methods is overcome and spectral-like resolution of the MLC scheme is observed. The dissipative, dispersive, and anisotropic error of the MLC scheme is much smaller than that of conventional finite difference methods. Compared with Zhong's fifth-order explicit scheme, both the seventh-order 2-2-2-2 scheme and third-order 1-1-1-1 scheme have a much better resolution in the large wavenumber region. Besides, the stencils are more compact because of more degrees of freedom on each grid point. Benefiting from the compactness, high-order stable boundary closure schemes can be attained. From both Fourier and stability analysis, the seventh-order 2-2-2-2 scheme with an α value of 12 is supposed to have the best accuracy, and it should be coupled with sixth-order boundary closure schemes for stability.

It should be emphasized that the spectral-like resolution is not simply caused by more total information, including values and derivatives, contained in the stencil. For example, the 3rd-order 1-1-1-1 scheme has a total of 6 points within a double-layer stencil. As a comparison, Zhong's 5th-order explicit scheme has a total of 7 points within a mono-layer stencil. However, the 1-1-1-1 scheme with less total information has much better spectral resolution than Zhong's 5th-order scheme, as shown in Fig. 16. Therefore, the multi-layer framework is the main reason for which the spectral resolution is significantly improved in the MLC schemes. In theory, more layers can be used in the MLC schemes, which means introducing additional equations for higher derivatives. The benefit is that the spectral resolution and the order of accuracy can be further improved with more degrees of freedom. However, the resulting scheme could be very stiff, and the formulation will be too complicated for nonlinear equations such as the Euler and Navier-Stokes equations. Both the stiffness and the complexity will probably affect the computational efficiency.

Overall our MLC scheme is promising due to very high-order of accuracy, spectral-like resolution, and consistent stability in one-dimensional cases. On the other hand, it shows weak numerical instabilities for a small range of wavenumbers when it is applied to multi-dimensional flows, which are mainly triggered by the inconsistency between its one and two-dimensional formulations. We have subsequently shown that the instability could lead to divergence in long-time multi-dimensional simulations. Moreover, the cross-derivative approximation in the MLC scheme requires an ad-hoc selection of supporting grid points, and the cross-derivative approximation is relatively inefficient for very high-order cases. To address the remaining challenges of the MLC scheme and achieve better performance for multi-dimensional flow simulations, we have also developed another two new, i.e. the directional multi-layer compact (DMLC) scheme, and the least square multi-layer compact (LSMLC) scheme.

5 Personnel

The following personnel conduct research for the grant and are partially supported by the grant:

1. Principal Investigator: Professor Xiaolin Zhong
2. Ph.D. Students: Zeyu Bai, Danny Fong, Chris Haley, and Carleton Knisely

6 Publications

Ph.D. Theses:

- 1 K. D. Fong, "A Numerical Study of 2-D Surface Roughness Effects on the Growth of Wave Modes in Hypersonic Boundary Layers," Ph.D. Thesis in Mechanical Engineering, UCLA, 2017.
- 2 C. P. Knisely, "Supersonic Unstable Modes in Hypersonic Boundary Layers with Thermochemical Nonequilibrium Effects," Ph.D. Thesis in Aerospace Engineering, UCLA, 2018.
- 3 Z. Bai, "*New Multi-Layer Compact High-Order Finite Difference Methods with Spectral-Like Resolution for Compressible Flow Simulations*," Ph.D. Thesis in Mechanical Engineering, UCLA, 2019.

In Archival Journals:

- 4 Z. Bai and X. Zhong, "New very high-order upwind multi-layer compact (MLC) schemes with spectral-like resolution for flow simulations," *Journal of Computational Physics*, 378:63-109, 2019.

- 5 C. Knisely and X. Zhong, "Sound radiation by supersonic unstable modes in hypersonic blunt cone boundary layers. I. Linear stability theory", *Physics of Fluids*, 31:024103, 2019.
- 6 C. Knisely and X. Zhong, "Sound radiation by supersonic unstable modes in hypersonic blunt cone boundary layers. II. Direct numerical simulation", *Physics of Fluids*, 31: 024104, 2019.
- 7 C. Knisely and X. Zhong, "Significant Supersonic Modes and the Wall Temperature Effect in Hypersonic Boundary Layers", *AIAA Journal*, 57(4):1552-1566, 2019.
- 8 P. T. Greene, J. D. Eldredge, X. Zhong, and J. Kim, "A high-order multi-zone cut-stencil method for numerical simulations of high-speed flows over complex geometries," *Journal of Computational Physics*, Vol. 316, pp. 652-681. 2016.
- 9 C. H. Mortensen and X. Zhong, "Real-Gas and Surface-Ablation Effects on Hypersonic Boundary-Layer Instability over a Blunt Cone," *AIAA Journal*. Vol. 54, No. 3, pp. 976-994, 2016.

In Conference Proceedings:

- 10 Z. Bai and X. Zhong, "Very High-Order Upwind Multi-Layer Compact (MLC) Schemes with Spectral-Like Resolution II: Two-Dimensional Case", AIAA paper 2019-1398, January 2019.
- 11 C. Haley, K. Casper and X. Zhong, "Joint Numerical and Experimental Investigation of Roughness Effect on Hypersonic 2nd Mode Instability and Transition", AIAA paper 2019-0873, January 2019.
- 12 C. Knisely, C. Haley, and X. Zhong, "Impact of Conical Hypersonic Boundary Layer Transition on Skin Drag and Heating", AIAA SciTech Forum, AIAA 2019-1134, January 2019.
- 13 C. Knisely and X. Zhong, "Impact of Thermochemical Nonequilibrium Effects on the Supersonic Mode in Hypersonic Boundary Layers", AIAA SciTech Forum, AIAA 2019-1132, January 2019.
- 14 C. P. Knisely and X. Zhong, "The Supersonic Mode and the Role of Wall Temperature in Hypersonic Boundary Layers with Thermochemical Nonequilibrium Effects," AIAA paper 2018-3218, June 2018.
- 15 C. P. Knisely and X. Zhong, "Supersonic Modes in Hot-Wall Hypersonic Boundary Layers with Thermochemical Nonequilibrium Effects," AIAA paper 2018-2085, January 2018.

- 16 C. Haley and X. Zhong, "Direct Numerical Simulation of Hypersonic Flow over a Blunt Cone with Axisymmetric Isolated Roughness," AIAA paper 2017-4514, June 2017.
- 17 C. P. Knisely and X. Zhong, "An Investigation of Sound Radiation by Supersonic Unstable Modes in Hypersonic Boundary Layers," AIAA paper 2017-4516, June 2017.
- 18 Z. Bai and X. Zhong, "New Very High-Order Upwind Multilayer Compact Schemes with Spectral-Like Resolution for Flow Simulations", AIAA paper 2017-0518, January 2017.
- 19 M. Miselis, Y. Huang, and X. Zhong, "Modal Analysis of Receptivity Mechanisms for a Freestream Hot-Spot Perturbation on a Blunt Compression-Cone Boundary Layer," AIAA paper 2016-3345, June 2016.
- 20 K.D. Fong, X. Wang, and X. Zhong, " DNS and PSE study on the stabilization effect of hypersonic boundary layer waves using 2-D surface roughness," AIAA paper 2016-3347, June 2016.
- 21 C. Mortensen and X. Zhong, "Numerical Simulation of Hypersonic Boundary-Layer Instability in a Real Gas with Two-Dimensional Surface Roughness", AIAA paper 2015-3077, June 2015.
- 22 K.D. Fong, X. Wang, and X. Zhong, "Parametric Study on Stabilization of Hypersonic Boundary-Layer Waves Using 2-D Surface Roughness", AIAA paper 2015-0837, January 2015.

7 Acknowledgement / Disclaimer

This work was sponsored by the Air Force Office of Scientific Research, USAF, under AFOSR Grant #FA9550-15-1-0268. The program manager is Dr. Ivett Leyva. The views and conclusions contained herein are those of the author and should not be interpreted as necessarily representing the official policies or endorsements either expressed or implied, of the Air Force Office of Scientific Research or the U.S. Government.

8 References

- [1] R.L. Kimmel, Aspects of Hypersonic Boundary-Layer Transition Control, in: 41st Aerosp. Sci. Meet. Exhib., American Institute of Aeronautics and Astronautics, Reno, Nevada, 2003: p. 772. doi:10.2514/6.2003-772.
- [2] X. Zhong, X. Wang, Direct Numerical Simulation on the Receptivity, Instability, and Transition of Hypersonic Boundary Layers, *Annu. Rev. Fluid Mech.* 44 (2012) 527–561. doi:10.1146/annurev-fluid-120710-101208.
- [3] T. Ishihara, T. Gotoh, Y. Kaneda, Study of High–Reynolds Number Isotropic Turbulence by Direct Numerical Simulation, *Annu. Rev. Fluid Mech.* 41 (2009) 165–180. doi:10.1146/annurev.fluid.010908.165203.
- [4] P. Moin, K. Mahesh, DIRECT NUMERICAL SIMULATION: A Tool in Turbulence Research, *Annu. Rev. Fluid Mech.* 30 (1998) 539–578. doi:10.1146/annurev.fluid.30.1.539.
- [5] C.K.W. Tam, Computational Aeroacoustics - Issues and Methods, *AIAA J.* 33 (1995) 1788–1796. doi:10.2514/3.12728.
- [6] C. Bogey, C. Bailly, A family of low dispersive and low dissipative explicit schemes for flow and noise computations, *J. Comput. Phys.* 194 (2004) 194–214. doi:10.1016/j.jcp.2003.09.003.
- [7] G. Alfonsi, On Direct Numerical Simulation of Turbulent Flows, *Appl. Mech. Rev.* 64 (2011) 020802. doi:10.1115/1.4005282.
- [8] V.L. Wells, R.A. Renaut, Computing Aerodynamically Generated Noise, *Annu. Rev. Fluid Mech.* 29 (1997) 161–199. doi:10.1146/annurev.fluid.29.1.161.
- [9] M. Wang, J.B. Freund, S.K. Lele, Computational Prediction of Flow-Generated Sound, *Annu. Rev. Fluid Mech.* 38 (2006) 483–512. doi:10.1146/annurev.fluid.38.050304.092036.
- [10] C.-W. Shu, High order WENO and DG methods for time-dependent convection-dominated PDEs: A brief survey of several recent developments, *J. Comput. Phys.* 316 (2016) 598–613. doi:10.1016/j.jcp.2016.04.030.
- [11] J.A. Ekaterinaris, High-order accurate, low numerical diffusion methods for aerodynamics, *Prog. Aerosp. Sci.* 41 (2005) 192–300. doi:10.1016/j.paerosci.2005.03.003.
- [12] Z.J. Wang, High-order methods for the Euler and Navier–Stokes equations on unstructured grids, *Prog. Aerosp. Sci.* 43 (2007) 1–41. doi:10.1016/j.paerosci.2007.05.001.
- [13] M. Dubiner, Spectral Methods on Triangles and Other Domains, *J. Sci. Comput.* 6 (1991) 345–390. doi:10.1007/BF01060030.
- [14] R.D. Moser, P. Moin, A. Leonard, A Spectral Numerical Method for the Navier-Stokes Equations with Applications to Taylor-Couette Flow, *J. Comput. Phys.* 52 (1983) 524–544. doi:10.1016/0021-9991(83)90006-2.
- [15] M.Y. Hussaini, T.A. Zang, Spectral Methods in Fluid Dynamics, *Annu. Rev. Fluid Mech.* 19 (1987) 339–367. doi:10.1146/annurev.fl.19.010187.002011.
- [16] B. Cockburn, S.-Y. Lin, C.-W. Shu, TVB Runge-Kutta Local Projection Discontinuous Galerkin Finite Element Method for Conservation Laws III: One-Dimensional Systems, *J. Comput. Phys.* 84 (1989) 90–113. doi:10.1016/0021-9991(89)90183-6.
- [17] B. Cockburn, C.-W. Shu, The Runge–Kutta Discontinuous Galerkin Method for Conservation Laws V: Multidimensional Systems, *J. Comput. Phys.* 141 (1998) 199–224.

- doi:10.1006/jcph.1998.5892.
- [18] J. Qiu, M. Dumbser, C.-W. Shu, The discontinuous Galerkin method with Lax–Wendroff type time discretizations, *Comput. Methods Appl. Mech. Eng.* 194 (2005) 4528–4543. doi:10.1016/j.cma.2004.11.007.
- [19] J. Zhu, X. Zhong, C.-W. Shu, J. Qiu, Runge–Kutta discontinuous Galerkin method using a new type of WENO limiters on unstructured meshes, *J. Comput. Phys.* 248 (2013) 200–220. doi:10.1016/j.jcp.2013.04.012.
- [20] S.K. Lele, Compact Finite Difference Schemes with Spectral-like Resolution, *J. Comput. Phys.* 103 (1992) 16–42. doi:10.1016/0021-9991(92)90324-R.
- [21] X. Zhong, High-Order Finite-Difference Schemes for Numerical Simulation of Hypersonic Boundary-Layer Transition, *J. Comput. Phys.* 144 (1998) 662–709. doi:10.1006/jcph.1998.6010.
- [22] K. Mahesh, A Family of High Order Finite Difference Schemes with Good Spectral Resolution, *J. Comput. Phys.* 145 (1998) 332–358. doi:10.1006/jcph.1998.6022.
- [23] R.K. Shukla, X. Zhong, Derivation of high-order compact finite difference schemes for non-uniform grid using polynomial interpolation, *J. Comput. Phys.* 204 (2005) 404–429. doi:10.1016/j.jcp.2004.10.014.
- [24] R.K. Shukla, M. Tatineni, X. Zhong, Very high-order compact finite difference schemes on non-uniform grids for incompressible Navier–Stokes equations, *J. Comput. Phys.* 224 (2007) 1064–1094. doi:10.1016/j.jcp.2006.11.007.
- [25] P.C. Chu, C. Fan, A Three-Point Combined Compact Difference Scheme, *J. Comput. Phys.* 140 (1998) 370–399. doi:10.1006/jcph.1998.5899.
- [26] H.C. Yee, N.D. Sandham, M.J. Djomehri, Low-Dissipative High-Order Shock-Capturing Methods Using Characteristic-Based Filters, *J. Comput. Phys.* 150 (1999) 199–238. doi:10.1006/jcph.1998.6177.
- [27] A. Harten, High resolution schemes for hyperbolic conservation laws, *J. Comput. Phys.* 49 (1983) 357–393. doi:10.1016/0021-9991(83)90136-5.
- [28] A. Harten, B. Engquist, S. Osher, S.R. Chakravarthy, Uniformly high order accurate essentially non-oscillatory schemes, III, *J. Comput. Phys.* 71 (1987) 231–303. doi:10.1016/0021-9991(87)90031-3.
- [29] X.-D. Liu, S. Osher, T. Chan, Weighted Essentially Non-oscillatory Schemes, *J. Comput. Phys.* 115 (1994) 200–212. doi:10.1006/jcph.1994.1187.
- [30] G.-S. Jiang, C.-W. Shu, Efficient Implementation of Weighted ENO Schemes, *J. Comput. Phys.* 126 (1996) 202–228. doi:10.1006/jcph.1996.0130.
- [31] Y.-X. Ren, M. Liu, H. Zhang, A characteristic-wise hybrid compact-WENO scheme for solving hyperbolic conservation laws, *J. Comput. Phys.* 192 (2003) 365–386. doi:10.1016/j.jcp.2003.07.006.
- [32] L. Zhang, W. Liu, L. He, X. Deng, H. Zhang, A class of hybrid DG/FV methods for conservation laws I: Basic formulation and one-dimensional systems, *J. Comput. Phys.* 231 (2012) 1081–1103. doi:10.1016/j.jcp.2011.06.010.
- [33] L. Zhang, W. Liu, L. He, X. Deng, H. Zhang, A class of hybrid DG/FV methods for conservation laws II: Two-dimensional cases, *J. Comput. Phys.* 231 (2012) 1104–1120. doi:10.1016/j.jcp.2011.03.032.

- [34] J.J. Choi, Hybrid spectral difference/embedded finite volume method for conservation laws, *J. Comput. Phys.* 295 (2015) 285–306. doi:10.1016/j.jcp.2015.04.013.
- [35] Y. Liu, M. Vinokur, Z.J. Wang, Spectral difference method for unstructured grids I: Basic formulation, *J. Comput. Phys.* 216 (2006) 780–801. doi:10.1016/j.jcp.2006.01.024.
- [36] Z.J. Wang, Y. Liu, G. May, A. Jameson, Spectral Difference Method for Unstructured Grids II: Extension to the Euler Equations, *J. Sci. Comput.* 32 (2007) 45–71. doi:10.1007/s10915-006-9113-9.
- [37] A. Balan, G. May, J. Schöberl, A stable high-order Spectral Difference method for hyperbolic conservation laws on triangular elements, *J. Comput. Phys.* 231 (2012) 2359–2375. doi:10.1016/j.jcp.2011.11.041.
- [38] Z.J. Wang, Spectral (Finite) Volume Method for Conservation Laws on Unstructured Grids: Basic Formulation, *J. Comput. Phys.* 178 (2002) 210–251. doi:10.1006/jcph.2002.7041.
- [39] Y. Liu, M. Vinokur, Z.J. Wang, Spectral (finite) volume method for conservation laws on unstructured grids V: Extension to three-dimensional systems, *J. Comput. Phys.* 212 (2006) 454–472. doi:10.1016/j.jcp.2005.06.024.
- [40] Y. Sun, Z.J. Wang, Y. Liu, Spectral (finite) volume method for conservation laws on unstructured grids VI: Extension to viscous flow, *J. Comput. Phys.* 215 (2006) 41–58. doi:10.1016/j.jcp.2005.10.019.
- [41] Z.J. Wang, Y. Liu, Extension of the spectral volume method to high-order boundary representation, *J. Comput. Phys.* 211 (2006) 154–178. doi:10.1016/j.jcp.2005.05.022.
- [42] Z. Haras, S. Ta’asan, Finite difference schemes for long-time integration, *J. Comput. Phys.* 114 (1994) 265–279. doi:10.1006/jcph.1994.1165.
- [43] G. Ashcroft, X. Zhang, Optimized prefactored compact schemes, *J. Comput. Phys.* 190 (2003) 459–477. doi:10.1016/S0021-9991(03)00293-6.
- [44] R. Hixon, Prefactored Small-Stencil Compact Schemes, *J. Comput. Phys.* 165 (2000) 522–541. doi:10.1006/jcph.2000.6631.
- [45] J.W. Kim, D.J. Lee, Optimized Compact Finite Difference Schemes with Maximum Resolution, *AIAA J.* 34 (1996) 887–893. doi:10.2514/3.13164.
- [46] X. Liu, S. Zhang, H. Zhang, C.-W. Shu, A new class of central compact schemes with spectral-like resolution I: Linear schemes, *J. Comput. Phys.* 248 (2013) 235–256. doi:10.1016/j.jcp.2013.04.014.
- [47] P.C. Chu, C. Fan, A Three-Point Sixth-Order Nonuniform Combined Compact Difference Scheme, *J. Comput. Phys.* 148 (1999) 663–674. doi:10.1006/jcph.1998.6141.
- [48] Y.G. Bhumkar, T.W.H. Sheu, T.K. Sengupta, A dispersion relation preserving optimized upwind compact difference scheme for high accuracy flow simulations, *J. Comput. Phys.* 278 (2014) 378–399. doi:10.1016/j.jcp.2014.08.040.
- [49] C. Cheong, S. Lee, Grid-Optimized Dispersion-Relation-Preserving Schemes on General Geometries for Computational Aeroacoustics, *J. Comput. Phys.* 174 (2001) 248–276. doi:10.1006/jcph.2001.6904.
- [50] M.K. Rajpoot, T.K. Sengupta, P.K. Dutt, Optimal time advancing dispersion relation preserving schemes, *J. Comput. Phys.* 229 (2010) 3623–3651. doi:10.1016/j.jcp.2010.01.018.
- [51] T.K. Sengupta, V. Lakshmanan, V.V.S.N. Vijay, A new combined stable and dispersion relation preserving compact scheme for non-periodic problems, *J. Comput. Phys.* 228 (2009) 3048–

3071. doi:10.1016/j.jcp.2009.01.003.
- [52] C.K.W. Tam, J.C. Webb, Dispersion-Relation-Preserving Finite Difference Schemes for Computational Acoustics, *J. Comput. Phys.* 107 (1993) 262–281. doi:10.1006/jcph.1993.1142.
- [53] G. Cunha, S. Redonnet, On the effective accuracy of spectral-like optimized finite-difference schemes for computational aeroacoustics, *J. Comput. Phys.* 263 (2014) 222–232. doi:10.1016/j.jcp.2014.01.024.
- [54] X. Zhong, M. Tatineni, High-order non-uniform grid schemes for numerical simulation of hypersonic boundary-layer stability and transition, *J. Comput. Phys.* 190 (2003) 419–458. doi:10.1016/S0021-9991(03)00282-1.
- [55] S. Pirozzoli, On the spectral properties of shock-capturing schemes, *J. Comput. Phys.* 219 (2006) 489–497. doi:10.1016/j.jcp.2006.07.009.
- [56] S. Pirozzoli, Numerical Methods for High-Speed Flows, *Annu. Rev. Fluid Mech.* 43 (2011) 163–194. doi:10.1146/annurev-fluid-122109-160718.
- [57] C.-W. Shu, High Order Weighted Essentially Nonoscillatory Schemes for Convection Dominated Problems, *SIAM Rev.* 51 (2009) 82–126. doi:10.1137/070679065.
- [58] D.J. Hill, D.I. Pullin, Hybrid tuned center-difference-WENO method for large eddy simulations in the presence of strong shocks, *J. Comput. Phys.* 194 (2004) 435–450. doi:10.1016/j.jcp.2003.07.032.
- [59] E.M. Taylor, M. Wu, M.P. Martín, Optimization of nonlinear error for weighted essentially non-oscillatory methods in direct numerical simulations of compressible turbulence, *J. Comput. Phys.* 223 (2007) 384–397. doi:10.1016/j.jcp.2006.09.010.
- [60] M.D. Salas, *A Shock-Fitting Primer*, CRC Press, 2009.
- [61] A. Prakash, N. Parsons, X. Wang, X. Zhong, High-order shock-fitting methods for direct numerical simulation of hypersonic flow with chemical and thermal nonequilibrium, *J. Comput. Phys.* 230 (2011) 8474–8507. doi:10.1016/j.jcp.2011.08.001.
- [62] P.S. Rawat, X. Zhong, On high-order shock-fitting and front-tracking schemes for numerical simulation of shock–disturbance interactions, *J. Comput. Phys.* 229 (2010) 6744–6780. doi:10.1016/j.jcp.2010.05.021.
- [63] W.S. SARIC, GORTLER VORTICES, *Annu. Rev. Fluid Mech.* 26 (1994) 379–409. doi:10.1146/annurev.fluid.26.1.379.
- [64] W.S. Saric, H.L. Reed, E.J. Kerschen, Boundary-layer receptivity to freestream disturbances, *Annu. Rev. Fluid Mech.* 34 (2002) 291–319. doi:10.1146/annurev.fluid.34.082701.161921.
- [65] W.S. Saric, H.L. Reed, E.B. White, Stability and transition of three-dimensional boundary layers, *Annu. Rev. Fluid Mech.* 35 (2003) 413–440. doi:10.1146/annurev.fluid.35.101101.161045.
- [66] P.J. Schmid, Nonmodal stability theory, *Annu. Rev. Fluid Mech.* 39 (2007) 129–162. doi:10.1146/annurev.fluid.38.050304.092139.
- [67] Y.S. KACHANOV, PHYSICAL-MECHANISMS OF LAMINAR-BOUNDARY-LAYER TRANSITION, *Annu. Rev. Fluid Mech.* 26 (1994) 411–482. doi:10.1146/annurev.fluid.26.1.411.
- [68] T. HERBERT, SECONDARY INSTABILITY OF BOUNDARY-LAYERS, *Annu. Rev. Fluid Mech.* 20 (1988) 487–526.
- [69] P. Durbin, X. Wu, Transition beneath vortical disturbances, *Annu. Rev. Fluid Mech.* 39 (2007)

- 107–128. doi:10.1146/annurev.fluid.39.050905.110135.
- [70] M.E. GOLDSTEIN, L.S. HULTGREN, BOUNDARY-LAYER RECEPTIVITY TO LONG-WAVE FREE-STREAM DISTURBANCES, *Annu. Rev. Fluid Mech.* 21 (1989) 137–166. doi:10.1146/annurev.fl.21.010189.001033.
- [71] I. TANI, BOUNDARY-LAYER TRANSITION, *Annu. Rev. Fluid Mech.* 1 (1969) 169–. doi:10.1146/annurev.fl.01.010169.001125.
- [72] H.L. Reed, W.S. Saric, D. Arnal, Linear stability theory applied to boundary layers, *Annu. Rev. Fluid Mech.* 28 (1996) 389–428. doi:10.1146/annurev.fl.28.010196.002133.
- [73] S.P. Schneider, Flight data for boundary-layer transition at hypersonic and supersonic speeds, *J. Spacecr. Rockets.* 36 (1999) 8–20. doi:10.2514/2.3428.
- [74] S.P. Schneider, Effects of high-speed tunnel noise on laminar-turbulent transition, *J. Spacecr. Rockets.* 38 (2001) 323–333. doi:10.2514/2.3705.
- [75] S.P. Schneider, Laminar-turbulent transition on reentry capsules and planetary probes, *J. Spacecr. Rockets.* 43 (2006) 1153–1173. doi:10.2514/1.22594.
- [76] S.P. Schneider, Erratum on Laminar-Turbulent transition on reentry capsules and planetary probes (vol 43, pg 1153, 2006), *J. Spacecr. Rockets.* 44 (2007) 464–484. doi:10.2514/1.30727.
- [77] S.P. Schneider, Effects of roughness on hypersonic boundary-layer transition, *J. Spacecr. Rockets.* 45 (2008) 193–209. doi:10.2514/1.29713.
- [78] S.P. Schneider, Development of hypersonic quiet tunnels, *J. Spacecr. Rockets.* 45 (2008) 641–664. doi:10.2514/1.34489.
- [79] S.P. Schneider, Summary of Hypersonic Boundary-Layer Transition Experiments on Blunt Bodies with Roughness, *J. Spacecr. Rockets.* 45 (2008) 1090–1105. doi:10.2514/1.37431.
- [80] S.P. Schneider, Hypersonic Boundary-Layer Transition with Ablation and Blowing, *J. Spacecr. Rockets.* 47 (2010) 225–237. doi:10.2514/1.43926.
- [81] A. Fedorov, Transition and Stability of High-Speed Boundary Layers, in: Davis, SH and Moin, P (Ed.), *Annu. Rev. FLUID Mech. VOL 43, ANNUAL REVIEWS, 4139 EL CAMINO WAY, PO BOX 10139, PALO ALTO, CA 94303-0897 USA, 2011: pp. 79–95.* doi:10.1146/annurev-fluid-122109-160750.
- [82] L.M. MACK, LINEAR-STABILITY THEORY AND PROBLEM OF SUPERSONIC BOUNDARY-LAYER TRANSITION, *AIAA J.* 13 (1975) 278–289. doi:10.2514/3.49693.
- [83] L. KLEISER, T.A. ZANG, NUMERICAL-SIMULATION OF TRANSITION IN WALL-BOUNDED SHEAR FLOWS, *Annu. Rev. Fluid Mech.* 23 (1991) 495–537.
- [84] J. Qiu, C.-W. Shu, Hermite WENO schemes and their application as limiters for Runge–Kutta discontinuous Galerkin method: one-dimensional case, *J. Comput. Phys.* 193 (2004) 115–135. doi:10.1016/j.jcp.2003.07.026.
- [85] J. Qiu, C.-W. Shu, Hermite WENO schemes and their application as limiters for Runge–Kutta discontinuous Galerkin method II: Two dimensional case, *Comput. Fluids.* 34 (2005) 642–663. doi:10.1016/j.compfluid.2004.05.005.
- [86] J. Zhu, J. Qiu, Hermite WENO Schemes and Their Application as Limiters for Runge-Kutta Discontinuous Galerkin Method, III: Unstructured Meshes, *J. Sci. Comput.* 39 (2009) 293–321. doi:10.1007/s10915-009-9271-7.
- [87] D.S. Balsara, C. Altmann, C.-D. Munz, M. Dumbser, A sub-cell based indicator for troubled zones in RKDG schemes and a novel class of hybrid RKDG+HWENO schemes, *J. Comput.*

- Phys. 226 (2007) 586–620. doi:10.1016/j.jcp.2007.04.032.
- [88] H. Luo, J.D. Baum, R. Löhner, A Hermite WENO-based limiter for discontinuous Galerkin method on unstructured grids, *J. Comput. Phys.* 225 (2007) 686–713. doi:10.1016/j.jcp.2006.12.017.
- [89] H. Luo, Y. Xia, S. Li, R. Nourgaliev, C. Cai, A Hermite WENO reconstruction-based discontinuous Galerkin method for the Euler equations on tetrahedral grids, *J. Comput. Phys.* 231 (2012) 5489–5503. doi:10.1016/j.jcp.2012.05.011.
- [90] H. Luo, Y. Xia, S. Spiegel, R. Nourgaliev, Z. Jiang, A reconstructed discontinuous Galerkin method based on a Hierarchical WENO reconstruction for compressible flows on tetrahedral grids, *J. Comput. Phys.* 236 (2013) 477–492. doi:10.1016/j.jcp.2012.11.026.
- [91] S.-C. Chang, The Method of Space-Time Conservation Element and Solution Element—A New Approach for Solving the Navier-Stokes and Euler Equations, *J. Comput. Phys.* 119 (1995) 295–324. doi:10.1006/jcph.1995.1137.
- [92] S.-C. Chang, X.-Y. Wang, W.-M. To, Application of the Space-Time Conservation Element and Solution Element Method to One-Dimensional Convection-Diffusion Problems, *J. Comput. Phys.* 165 (2000) 189–215. doi:10.1006/jcph.2000.6610.
- [93] Z.-C. Zhang, S.T.J. Yu, S.-C. Chang, A Space-Time Conservation Element and Solution Element Method for Solving the Two- and Three-Dimensional Unsteady Euler Equations Using Quadrilateral and Hexahedral Meshes, *J. Comput. Phys.* 175 (2002) 168–199. doi:10.1006/jcph.2001.6934.
- [94] D. Shyam Sundar, K.S. Yeo, A high order meshless method with compact support, *J. Comput. Phys.* 272 (2014) 70–87. doi:10.1016/j.jcp.2014.04.010.
- [95] H. Nishikawa, A first-order system approach for diffusion equation. I: Second-order residual-distribution schemes, *J. Comput. Phys.* 227 (2007) 315–352. doi:10.1016/j.jcp.2007.07.029.
- [96] H. Nishikawa, A first-order system approach for diffusion equation. II: Unification of advection and diffusion, *J. Comput. Phys.* 229 (2010) 3989–4016. doi:10.1016/j.jcp.2009.10.040.
- [97] H. Nishikawa, First-, second-, and third-order finite-volume schemes for diffusion, *J. Comput. Phys.* 256 (2014) 791–805. doi:10.1016/j.jcp.2013.09.024.
- [98] H. Nishikawa, First, second, and third order finite-volume schemes for advection-diffusion, *J. Comput. Phys.* 273 (2014) 287–309. doi:10.1016/j.jcp.2014.05.021.
- [99] T.J. Poinso, S.K. Lele, Boundary conditions for direct simulations of compressible viscous flows, *J. Comput. Phys.* 101 (1992) 104–129. doi:10.1016/0021-9991(92)90046-2.